POLITECNICO DI TORINO

Corso di Laurea Magistrale in Ingegneria Aerospaziale

Tesi di Laurea Magistrale

Wing load reconstruction techniques and control algorithms for gust alleviation

Supervisors:
Prof. Marco Gherlone
Dott.ssa Elisa Capello

Candidate:
Andrea Maganuco

March 2019

A mamma e papà,
A nonna e la famiglia
Agli amici di Gela e Torino
Al nono piano
Al BOA XXVII
E a chi, dalla Russia al Portogallo,
mi ha motivato in questi anni
Grazie.

Abstract

The objective of this thesis is to find a method to reduce stresses and strains on a wing structure, due to non-static external loads, i.e. disturbances gust, through the deflection of the control surfaces. The control system, able to reduce the generated loads and stresses, is designed to reduce the weight of the structure and to increase the life of the aircraft components.

A preliminary research on previous works is required to understand different methods and tools, focusing on the hardware devices. With these devices the deformations of the structure can be measured in some crucial points, thus obtaining the strains and, as consequence, the displacements. Next, the complete FEM model is created. This model is then reduced in an equivalent one, describing various type of loads, concentrated and distributed. A methodology for the definition of the reduced model is derived and defining the various loads applied, the results of the simplified version are compared with the one of the detailed model. In a similar way, a methodology for the evaluation of the external loads is derived, following two steps: (1) the load reconstruction and (2) the data optimization. This last point is deeply discussed and a new methodology for the data collecting is proposed, limiting the number of data collectors.

Finally focusing on concentrated loads, a closed loop system is designed and a linear quadratic regulator (LQR) is proposed as control strategy. The objective of this control system is to reduce the internal stresses of the structure when a gust occur by aileron deflection.

Sommario

L'obiettivo di questa tesi è quello di trovare un metodo per ridurre le tensioni e le deformazioni di una struttura alare, dovuti a dei carichi non statici, i.e. carichi di raffica, attraverso la deflessione delle superfici di controllo. Il sistema di controllo, capace di ridurre i le tensioni e i carichi denerati, è progettato per ridurre il peso della struttura e di incrementare la vita dei componenti dell'aeromobile.

Una ricerca preliminare su lavori precedenti si è resa necessaria per comprendere i vari metodi e strumenti necessari, focalizzandosi sui device hardware. Con questi strumenti le deformazioni della struttura possono essere misurate, in punti particolamente critici, ottenendo quindi le deformazioni e, conseguentemente, gli spostamenti. In seguito, è stato creato il modello FEM completo. Questo modello è poi ridotto ad uno equivalente, descrivendo inoltre i vari tipi di carico applicati, concentrati e distribuiti. Una metodologia per la definizione del modello ridotto è stata derivata e definendo i vari carichi applicati, i risultati per il modello ridotto sono confrontati con quelli del modello di dettaglio. In un modo simile, un metodo per la valutazione dei carichi esterni è stato esposto, seguendo due step: (1) ricostruzione dei carichi e (2) ottimizzazione dei dati. Quest'ultimo punto è discusso a fondo e una nuova metodologia per l'acquisizione di dati è proposta, atta a limitare il numero degli strumenti di misura necessari.

Infine, focalizzandosi sui carichi concentrati, un sistema ad anello chiuso è stato definito e un Regolatore Quadratico Lineare (LQR) è stato proposto per il controllo. L'obiettivo del sistema di controllo è quello dir idurre le tensioni interne alla struttura in presenza di carichi da raffica, attraverso la deflessione degli alettoni.

Contents

List of Tables

List of Figures

Chapter 1

Introduction

Since the aerospace field has always been focused on the optimization of weights and performance, always keeping in mind the costs and the time of maintenance, in recent years, new methods of construction or design have been progressively made, allowing the use of lighter structures, which are continuously monitored to evaluate their health and to schedule maintenance or replacement. In this field it is of particular interest an active aircraft Structure Health Monitoring (SHM), which can be useful for the continuous monitoring of the structure through the use of tools like strain gauges or new fiber optic's sensors which can be installed on the structure to reconstruct deformations in the crucial points. Several studies have been carried out for the analysis of the use of these tools for the reconstruction of deformations and their installation on the structures as investigated in the SARISTU project (2016) [17], and in [21]. The object of this thesis is to exploit the possibility of knowing the deformations that these measuring instruments introduce, in order to be able to calculate the forces acting on the wing structure, which once known it is possible to limit the effect with the use of the mobile surfaces of the wing itself. The work carried out within this thesis can be divided into 3 parts, concerning the construction and definition of the models used, the reconstruction of the loads and the actual control. Chapter 2 discusses the various types of hardware that can be used for the measurement of deformations and accelerations, i.e. strain gauges, FBGs and accelerometers, with consequent operating principles and governing laws, and how can also be obtained information regarding the position and displacements of the components, also illustrating the characteristics and limitations of these components.

In chapter 3 the FEM models are described, which are used in this thesis for data on which to perform the study, since the method involves the use of the real structure of the aircraft, thus illustrating the model of the complete wing box and the concentrated one used for the control. Precisely for the latter are then illustrated the procedures for obtaining the mass, stiffness and damping matrices necessary for the construction of the model. In this chapter are exposed the loads to which the structure will be subject to reconstruction, and will explain the reasons that lead us to carry out the reconstruction with two load models, the concentrated one and the distributed one.

In chapter 4, the principle of reconstruction is illustrated, referring to Skopinski (1953) [22], through which is it possible to correlate the deformations within the structure with the external loads applied, and is exposed the algorithm that defines the number and the position of the data collectors to achieve this reconstruction. We then move on to optimizing the data collectors in order to have a limited number of the same without losing reliability in the reconstruction, illustrating how the loads were obtained in the case of concentrated and distributed values, the latter through the definition of basic functions.

Finally, in chapter 5 the control is given, defining gust loads, how the control is carried out by the deflection of the wing's mobile surfaces, the type of control through a Linear Quadratic Controller, and how our second order system is defined and reduced to two systems of the first order, controlling also stability and controllability, then concluding with the results deriving from the control.

Chapter 2

Methods for data collecting

The main purpose of this thesis, as previously explained in the overview, is to find a way to control stresses and strains inside a structure, in particular the wingbox one, in order to find a correlation between the deformations, inside the structure in one or multiple points, the forces applied to it and the related strains. From this point of view it is necessary an hardware support able to record the strains in real time, so they can be processed by a software and, through the ailerons deflection, being controlled. This leads to the introduction within the model of the strain gages and accelerometers, the latter being introduced for various reasons, explained later in this chapter.

2.1 Strain Gages

The use of strain gage technology in aerospace applications has a long history. Strain gages are bonded directly inside the structure, to measure stresses along load paths for wing deflection. The continuous increasing of the use of composite materials in the aerospace industry, combined with the need to have structures that can be monitored in order to reduce production and maintenance costs, has led in recent years to the introduction of new methods for investigating the health of such structures, not only in the aerospace industry.

From the historical point of view of this type of instrumentation, the

first strain gages were analogical, with components made up of springs and levers, which however did not provide great precision. Subsequently there was the introduction of strain gages based on the material's resistive properties , exploiting the variation of resistance within a conductive material if subjected to mechanical stresses. Over recent decades, especially after the NASA development, strain gages based on an optical technology through the optical fibers have been introduced, taking advantage of optical properties.

This field includes fiber optic ribbon tapes (FORTs), which are particularly suitable to be used in composite structures as they can be installed between the various layers, without introducing particular findings from a structural point of view, but they can also be applied on the surface, as in the classical method. Compared to the classic Electrical Strain Gages they bring not a few notable improvements, so they can be considered the state-of-art for this type of structural investigation: first of all, they can be arranged inside the structure, inserting them inside the composite structure in the autoclave phase, or attached with special glues on the surfaces, still obtaining excellent results. Compared to the classic ESGs they are much more resistant to fatigue loads analysis where the structure is stressed to an high number of cycles, since the sensor does not detach from the structure after a certain number of cycles.

2.1.1   Electrical Strain Gages

The classic electrical strain gages (ESG) are measuring instruments used to detect small deformations inside the structure of a component subjected to mechanical or thermic stresses; these deformations are obtained from the knowledge of the behaviour and of the mechanical/physical material's characteristics. Basically, electrical strain gauges, consist of a thin metal wire, which is rigidly applied to a plastic material support. It is installed directly on the surface of the object with a suitable glue, suffering its same deformations: it is precisely this feature that allows us to measure the strains, since that, by lengthening or shortening, dimensional variations are created in the wire so that its electrical resistance varies, and through the use of a wheatstone bridge, is it possible to measure the variation of electrical resistance and therefore the deformation.

As we can observe from fig.2.1 the metallic wire is positioned on parallel
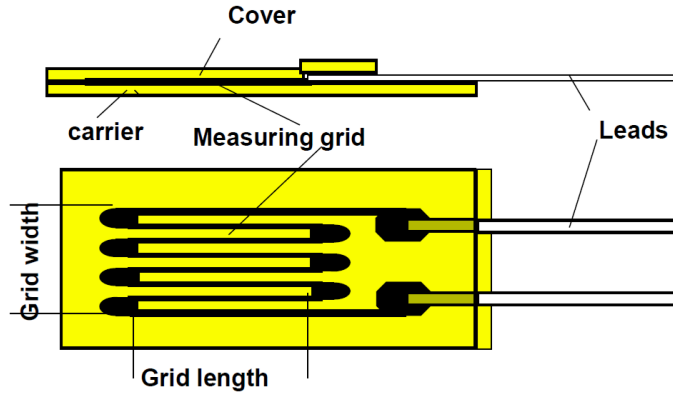
Figure 2.1.   Classical ESG component

rows, so to maximize the deformation's effect in order to have a more precise measurement. As can be imagined, the strain gauge is characterized by the resistance of the wire that constitutes the grid and by a factor which relates its resistance to the wire's length variation, which takes the name of Gauge factor G_F, that represent the sensitivity of the strain gauge, expressed as

$$G_F = \frac{\Delta R/R}{\Delta L/L} \tag{2.1}$$

Given the electrical resistance of the wire

$$R = \frac{\rho L}{A} \tag{2.2}$$

where R is the electrical resistance of the material which constitute the wire, L is the conductor length, A is the section area of the conductor and ρ is the material resistivity, if we differentiate the 2.2 we obtain

$$dR = \frac{\rho dL}{A} + \frac{d\rho L}{A} - \frac{d\rho dL}{A^2} \tag{2.3}$$

and being able to write the variation of volume of the material in case of small variations, having that $dL/L = \varepsilon$, as

5

$$dV = LdA + AdL = LA - L_0A_0 = L(1 + \varepsilon) \cdot A(1 - \nu\varepsilon)^2 \tag{2.4}$$

and substituting the 2.4 in 2.2, with some mathematical steps, we get

$$\frac{dR/R}{\varepsilon} = 1 + 2\nu + \frac{d\rho/\rho}{\varepsilon} \tag{2.5}$$

thus obtaining that the Gage Factor G_F can also be expressed as

$$G_F = 1 + 2\nu + \frac{d\rho/\rho}{\varepsilon} \tag{2.6}$$

where the first two components express the dependence on the deformation, while the last one represent the effect of the variation of specific resistivity. In this way is it possible to write the relationship that is used for the strain gauges

$$\frac{\Delta R}{R} = G_F \cdot \varepsilon \tag{2.7}$$

which binds the variation in resistance to deformation of the strain gauge's metal wire.

Since resistance variations are usually very small, the Wheatstone bridge is used to convert the variation of resistance into voltage variation, so that they can be amplified to allow the measurement.

Considering

$$V_0 = \frac{R_1 R_3 - R_4 R_2}{(R_2 + R_1)(R_3 + R_4)} V_e \tag{2.8}$$

we have that the variation of one of the resistances varies the V_0 tension's value, so differentiating the equation 2.8 on the basis of the 4 resistances , we get

$$\frac{R_1}{R_2} = \frac{R_4}{R_3}$$

$$R_1 R_3 = R_2 R_4$$
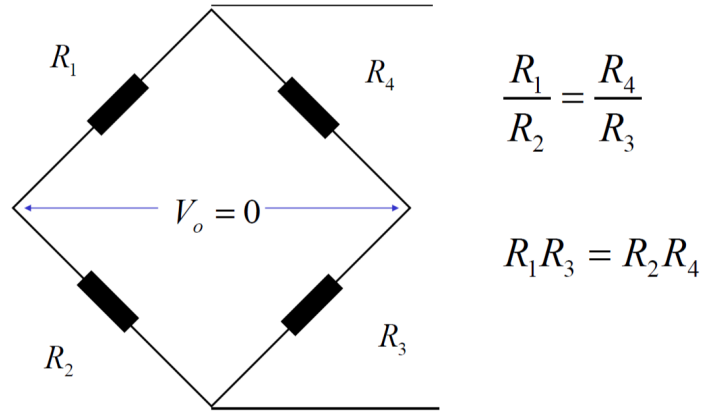
Figure 2.2.   Wheatstone bridge scheme

$$\frac{V_0}{V_e} = \frac{1}{4}\left[\frac{\Delta R_1}{R_1} - \frac{\Delta R_2}{R_2} + \frac{\Delta R_3}{R_3} - \frac{\Delta R_4}{R_4}\right] = \frac{G_F}{4}\left[\varepsilon_1 - \varepsilon_2 + \varepsilon_3 - \varepsilon_4\right] \quad (2.9)$$

By actively using 1,2 or all 4 strain gauges is it possible to measure the strain of the object under examination, being also able to perform a thermal deformation compensation, since, due to an appropriate positioning of the resistors, the deformation effect due to the temperature is compensated, and therefore the value of the deformation is due only to mechanical stresses.

Although they are widely used in laboratory tests, and are instruments with excellent precision, in the case of dynamic measurements, the use of this type of strain gauge is not the best choice: first of all, their connection to the object is made by gluing, and even if suitable glues are used, these glues can lose effectiveness over time and cause the strain gauge to detach from the object, thus losing the possibility of measuring the deformation; moreover the connection is made through conducting wires, which despite the low voltages, can lead to interference in the transmitted signal, as well as representing an additional weight on the structure in the event of a high number of applied strain gages

2.1.2   Fiber Bragg Gratings

A Fiber Bragg Grating (FBG) is a microstructure, which is typically few millimetres in length, that is photo inscribed in the core of a single mode fiber. This is obtained through a transverse illumination of the fiber with a UV laser beam and a mask, so to generate an interference pattern on its core, that will induce a permanent change in the physical characteristics of the silica matrix, that lead to a periodic modulation of the core index of refraction, creating a resonant structure [1] [2].
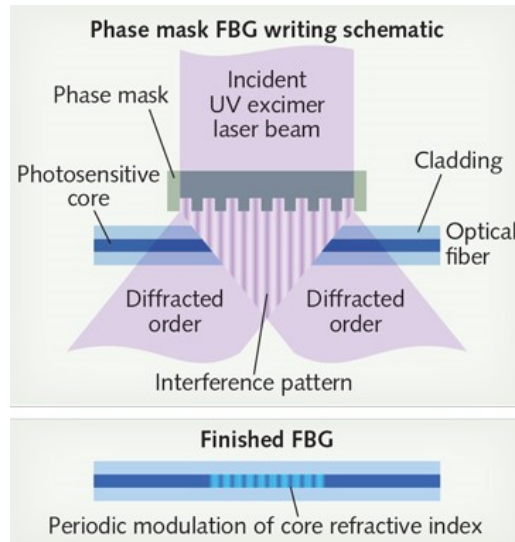
Figure 2.3.   Bragg grating inside the fiber, due to the incident laser beam

The resonant structure take the name of Bragg grating, which is able to reflect a precise wavelength, called Bragg wavelength λ_G, given by

$$\lambda_B = 2n_{eff}\Lambda \qquad (2.10)$$

where n_{eff} is the average refractive index and Λ is the grating period. When a thermal or mechanical load is applied to structure, the grating is strained, having a change in the peak of the reflected wavelength. Assuming therefore that there is no change of pressure, we can find that the variation of the reflex wavelength using the following equation:

$$\frac{\Delta\lambda_B}{\lambda_B} = \left[1 - \left(\frac{n_{eff}^2}{2}(p_{12} - \nu(p_{11} + p_{12}))\right)\right]\varepsilon + (a+\xi)\Delta T = F_G\varepsilon + (a+\xi)\Delta T$$

$$(2.11)$$

where $\Delta\lambda_B$ is the wavelength shift, λ_B is the initial reference wavelength, ν is the Poisson's ratio of the fiber, p_{11} and p_{12} are the elasto-optic coefficients of the elasto-optic tensor constants of the strain optic tensor and F_G represents in total the gage factor of the fiber; a is the coefficient of thermal expansion of the glass fiber, ξ is the fiber thermo-optic coefficient, and ΔT is the temperature change [3].
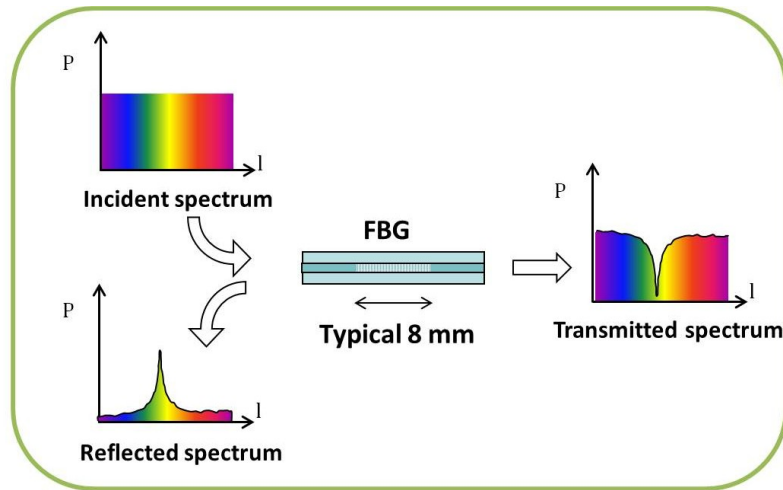
Figure 2.4. Reflected wavelength from the Bragg grating [3]

The technology of the FBG is used in the FORTs (Fiber Optic Ribbon Tapes) that are ribbon of optical fibers, formed in a flat strip. Are obtained through the manufacturing of a series of separates optical fibers laid down on a flat distribution, bonding them each other, using a special water tight tape material to hold them in their position. This type of cables are one of the best solutions when the installation has to be performed in tight places or with weight restrictions, as in the aerospace industry.

Those properties lead to the installation of those sensors in several type of structures, and in particular allow the installation either on the surface of the composite component of interest, or embedded inside their structure. This type of installation allow not only a constant knowledge about the displacements inside the structure, but also its heath doing so that could be
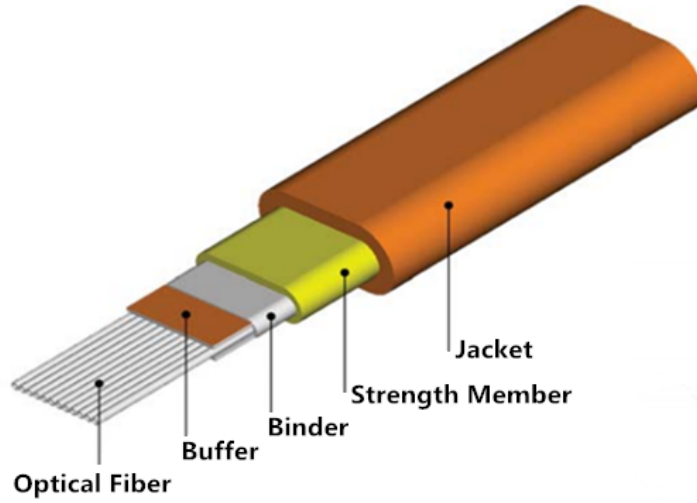
Figure 2.5.   FORT structure [4]

also utilized for a component approval or qualification. Despite its advantages the concept of the embedding could lead to a degrade of the mechanical properties of the structure, since the region of the material around the FBG is a potential site of damage initiation, but in several studies as [23] no decreased properties have been reported if the direction of the deployed fiber corresponds to the reinforcement one.

2.1.3   Displacement reconstruction

The real-time displacement prediction of the deformed structures is really important in the engineering applications, and considering the advantages introduced by the fiber bragg grating sensors, is it possible to reconstruct the dynamic deformation of a structure by the displacement got from the sensors. A method, investigated in [23], is based on a Kalman filter and the inverse Finite Element Method (iFEM). The iFEM method is based on the reconstruction of the displacement of a structure using the measurement obtained from strain sensors [5]. In this case is investigated a beam structure, developing a strain state equation of the structure using the finite element method (FEM), considering a model with $2n$ degrees of freedom, considering at each station w_n, vertical nodal displacement, and θ_n the nodal rotation, establishing a relationship between strain and nodal displacement as

$$\{\varepsilon\} = [B]\{\delta\} \tag{2.12}$$

where the coefficients inside the B matrix are given by the shape function

$$B(\xi) = \frac{1}{l^2}[l + 12\xi, l(-4 + 6\xi), 6 - 12\xi, l(-2 + 6\xi)]\frac{h}{2} \tag{2.13}$$

where l is the length of the beam element, $\xi = \frac{x}{l}$, and x is the location of the FBG in element. Having the eq. 2.12 we can get

$$\{\delta\} = [B]^{-1}\{\varepsilon\} \tag{2.14}$$

where δ and ε are $(2n \times 1)$ vectors and $[B]$ is an $(2n \times 2n)$ matrix. Considering the vibration equation of the beam, and substituting the eq. 2.14, multiplying left by $[B]^T$ we have

$$[M_s]\{\ddot{\delta}\} + [C_s]\{\dot{\delta}\} + [K_s]\{\delta\} = \{f\} \tag{2.15}$$

$$[B]^T[M_s][B]^{-1}\{\ddot{\varepsilon}\} + [B]^T[C_s][B]^{-1}\{\dot{\varepsilon}\} + [B]^T[K_s][B]^{-1}\{\varepsilon\} = [B]^T\{f\} \tag{2.16}$$

obtaining in this way a strain vibration equation as follow

$$[M_\varepsilon]\{\ddot{\varepsilon}\} + [C_\varepsilon]\{\dot{\varepsilon}\} + [K_\varepsilon]\{\varepsilon\} = \{f_\varepsilon\} \tag{2.17}$$

where the mass, damping and stiffness matrix are the one obtained in eq. 2.16 as $[B]^T[\cdot_s][B]^{-1}$. It's possible to write the state equation as

$$\dot{X}(t) = AX(t) + BF(t) \tag{2.18}$$

with

11

$$A = \begin{bmatrix} 0_{n \times n} & I_{n \times n} \\ -M_{\varepsilon}^{-1}K_{\varepsilon} & -M_{\varepsilon}^{-1}C_{\varepsilon} \end{bmatrix}$$

$$B = \begin{bmatrix} 0_{n \times n} \\ M_{\varepsilon}^{-1} \end{bmatrix}$$

$$X = \begin{bmatrix} \varepsilon \\ \dot{\varepsilon} \end{bmatrix}$$

The system is then discretized over time intervals Δt, becoming

$$X(k) = \Phi X(k-1) + \Gamma(F(k) + w(k)) \tag{2.19}$$

$$\Phi = exp(A * \Delta t) \tag{2.20}$$

$$\Gamma = \int_{(k-1)t}^{k\Delta t} exp[A(k\Delta t - \tau)]B d\tau \tag{2.21}$$

where $X(k)$ represents the state vector; Φ represents the state transition matrix; Γ represents the input matrix; Δt represents the sampling interval; $F(k)$ represents the load sequence. Then, Kalman filter is used to suppress vibrational dynamic noise.

At the last, iFEM is used to construct dynamic deformation, where the displacement vector are expressed by kinematic variables $u(x)$ and the kinematic variables are interpolated by element-shape function as

$$u(x) \approx u^e = N(x)q^e \tag{2.22}$$

where N is the shape-function matrix, q^e is the nodal degrees-of-freedom. Defining the strain field as $\varepsilon = \{\varepsilon_k\}$ the strain values can be expressed as

$$\varepsilon(u^e) = B(x)q^e \tag{2.23}$$

with B the shape-function matrix. After minimizing the least-square error between the analytic strain measure and the corresponding experimental strain measured at the n discrete locations by FBG sensors, it's possible to obtain the displacement vector, where the error functional is written as reported in [23] as

$$\Phi^e(u^e) = \parallel \varepsilon(u^e) - \varepsilon^e \parallel^2 \tag{2.24}$$

2.2 Accelerometers

An accelerometer is a measurement instrument able to detect and measure the acceleration, calculating the force on the object in comparison to its mass. The use of this type of transducers and sensors during the years is increasing, not only in the traditional applications as the scientific and aerospace fields, but also in several civil fields, really often used in combination with other sensors, as gyroscopes. There are several type of accelerometers but all of them is based on the same principle: calculating the inertia of a mass subjected to an acceleration, and due to this acceleration the mass moves from its initial position in a proportional way to the acceleration, having that the difference on the several types of accelerometers is based on the working principle of the sensor which detect the mass movement. Through the installation of an accelerometer on a structure is it possible to know the acceleration of the structure thanks to the inertia mass of the sensor, which reference system moves with the structure, calculating in this way the structure acceleration. The data form the accelerometer could be 1-D, having just one mass and a one dimensional movement detector, or 3-D, having one mass and three movement detector or three masses three different movement detectors, one for each axis of the orthogonal reference system.
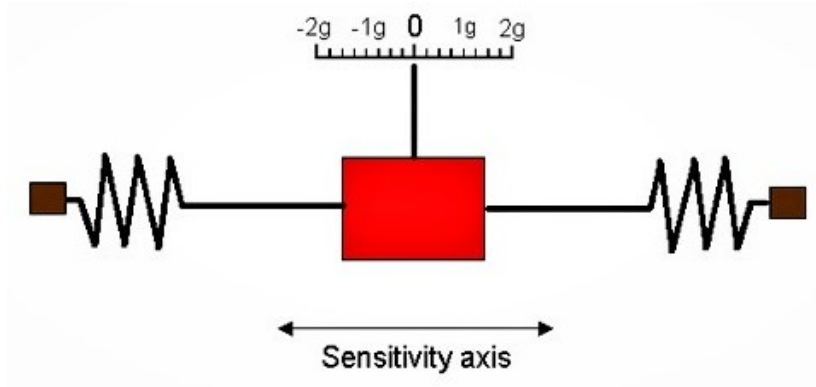
Figure 2.6.   Schematic accelerometer structure [6]

2.2.1   Displacement reconstruction

The accuracy in the estimation of the vibration characteristics and the possibility to reconstruct the velocities and displacements form the time signal makes the the accelerometers are some of the most frequently used sensors in the vibration response measurement for the structures. But this reconstruction it's quite difficult. Usually there are two ways in to convert measured time history of the acceleration signal into a displacement signal: one is to integrate directly le signal in the time domain, and the other one is by dividing the Fourier-transformed acceleration signal by the scale factor of $-\omega^2$ and taking its inverse Fourier transform. But both of these methods produce a significant amount of errors depending by the sampling resolution in the digitalization of the response signal. In [14] are discussed the problems involving the calculation of displacements from the acceleration recordings, so through double integration, and the amplification measurement errors of the input signal, with a correction of the errors thanks to a double integration introduced by an algorithm, and it's also shown that the main issues are due to the errors in the lower frequencies, so that the use of accelerometers capable to measure low frequency signal with high resolution was proposed and tested with quite reasonable results. In [10] both the ways to reconstruct the displacement are investigated, finding out that when the time signal of the acceleration is available and the Nyquist frequency of digitization is much higher than the highest frequency component of the signal, the direct double integration of the acceleration in the time domain provides reasonably accurate displacement time signal. When using the time domain method, the success of the reconstruction process depends

on the appropriate initial conditions during the double integration process. But if the frequency components of the measured acceleration signal are relatively high compared to the Nyquist frequency, the frequency domain method should be used. The effect of a double integration in the time domain is achieved by scaling the discrete Fourier transform of the measured acceleration signal in the frequency domain. The curve fitting around the peak values of the scale discrete Fourier transform provides a reasonably accurate shape of the Fourier transform of the original displacement signal. Is it possible, accordingly to the cited papers, to reconstruct the displacement from the acceleration signal with reasonable accurate results, so to reconstruct the displacements of some part of the structure during the flight.

Chapter 3

Models

Within this chapter, the models that have been created and will be used in the following chapters are shown and explained in detail. The first model, the detailed one, is a finite element model, realized using the MSC Patran/-Nastran 2018 software, whose task is to simulate the analysis structure behaviours and its response to the loads, and therefore to carry out the strains and the displacements that will be necessary during the reconstruction of the forces acting on the structure. It is also used to design the approximate beam-like model, through the reduction, where the structure is approximated to a series of beam elements, whose properties are extracted from the detailed model, and which will be necessary in the control phase. It will be used the reduced model because with this is possible to have a much lighter and faster system to be used during calculations, in order to be controlled quickly and with greater success, however not sacrificing the precision in the approximation of the behaviour. It will also be shown how the characteristics of mass, damping and stiffness necessary for the construction of the control system are obtained, which approximations regarding the loads were made, and some considerations about the independence of some degrees of freedom and the associated damping factors.

In the aeronautic field, the structures are designed taking into account in particular two key aspects: a maximum resistance, such as to be able to withstand the loads during flight, and a minimum weight, for propulsive reasons. These two aspects are bounded each other, as much of the weight of the aircraft is due to the structure, as well as its stiffness, which means that is it necessary to find the right compromise between the two properties.

For this reason in the aeronautical field there is a wide use of the half-shell structures, which are characterized by their ability to divide the different types of loads between the various elements within them, thus succeeding in reducing weight, as each component is specialized to absorb a type of load, and then optimized from the weight point of view to perform this task. In the half-shell model we can identify two main elements:

- **Panels**: structural elements, in which two dimensions are several orders of magnitude higher than a third one, which are specialized to withstand to shear stresses

- **Stringers**: structural elements, in which one dimension is several orders of magnitude higher than the other two, whose main function is to absorb axial loads on their surface, perpendicular to the axis of the main dimension

Through the combination of these two elements, aircraft structures are designed, and referring in particular to the wing, makes it possible to identify 4 main structures
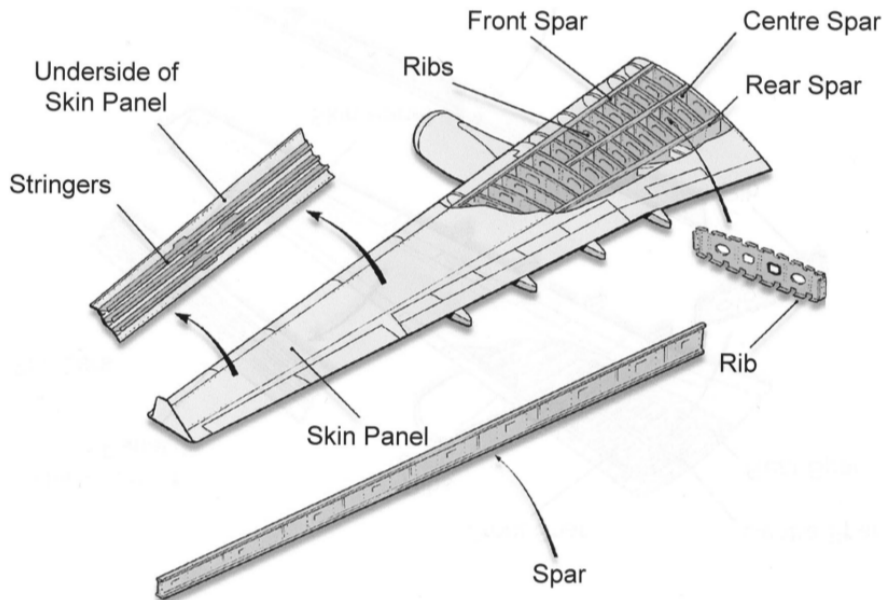
Figure 3.1.   Aircraft wing structure [20]

- **Spars**: the elements that run along the wingspan and whose main task is to withstand the bending. They are composed by two spar caps and a spar web, assimilating their shape to a double T, where the first ones have to withstand the axial loads along the wing, while the web spar, located in the middle, link them each other, transferring the shear stresses.

- **Ribs**: elements similar to the beams, are placed in a direction perpendicular to the spars and with a similar structure, with external reinforcements and a core, which task is to maintain the shape of the profile and to support it in areas with concentrated loads, such as engine attachment points or junctions with moving surfaces.

- **Skin Panels**: constitute the coating of the structure, that not only give the shape of the profile, but also contribute to the structural rigidity, ensuring torsional rigidity as they are able to withstand shear stresses.

- **Stringers**: longitudinal stiffening elements, connected with the panels and able to provide the stiffness for the compressing loads, to discharge part of the shear stresses in the form of normal stresses and to avoid instability of the panel due to the compression forces.

3.1 Detailed FEM Model

For the development of the complete FEM model, as mentioned in the introduction, the MSC Patran pre and post-processing software was used, through which the geometry and the finite elements model were defined. For the sizing of the model, different types of aircraft were taken into consideration, evaluating the profiles and dimensions of the wing structures, in particular commercial passenger transport aircraft, and taking inspiration from these structures, have been chosen, for the construction of the wing, the characteristics shown in the table 3.1

$(b/2)$	Wing span	$20\,\mathrm{m}$
(c_r)	Root chord	$5\,\mathrm{m}$
(c_t)	Tip chord	$1\,\mathrm{m}$
(t_r)	Profile thickness at the root section $0.25c$	$0.8\,\mathrm{m}$
(t_r)	Profile thickness at the tip section $0.25c$	$0.4\,\mathrm{m}$
$(\Lambda_{0.25_c})$	Sweep angle $0.25c$	$5.53°$
(Λ_{LE})	Sweep angle leading edge	$11.31°$
(Λ_{TE})	Sweep angle tailing edge	$0°$

Table 3.1.   Main values of the structure model

Following the values shown in table 3.1 the geometry of the structure was constructed, which is shown in fig.3.2.
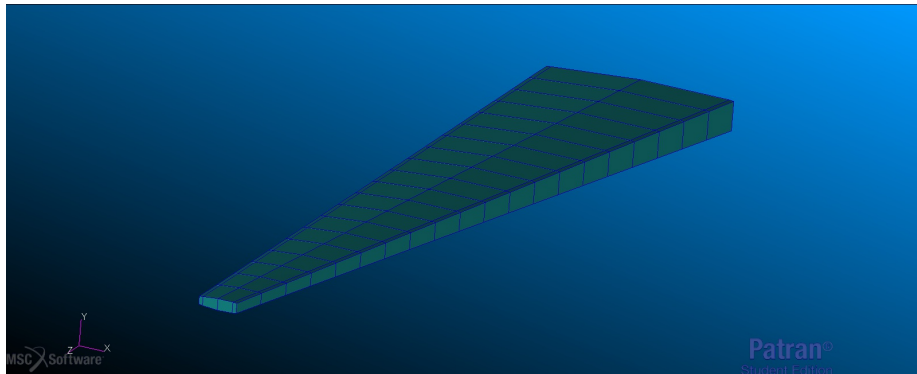
Figure 3.2.   Complete detailed FEM model
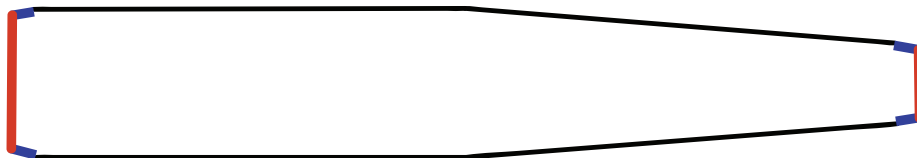
Figure 3.3.   Wing section - plane $x - y$

To this geometry has been associated a FEM mesh using, for all the elements excluding the stringers, the 4-node quadrangular elements, CQUAD4, according to the theory of Reissner-Mindlin, which unlike the Kirchoff-Love theory considers the effects of the shear stresses on the plate deformation. Using these elements the mesh was created manually, imposing a dimension on the elements, trying to impose an isometric geometry, which however is conditioned by the tapering of the chord along the wingspan accompanied by the need to hold a constant number of elements in each row. As regards the positioning of the ribs inside the structure, an equispaced insertion has been selected along the wing span, with the ribs spaced 1 m each other, for a total amount of 20 ribs, since in the root section no one has been inserted because the constraints will be applied to that section, and therefore would have been superfluous. Moreover, in order to further increase the rigidity of the structure, stringers were inserted along the wingspan, as well as from the theory of the half-shell, thus increasing the capacity of the structure to withstand the stresses.
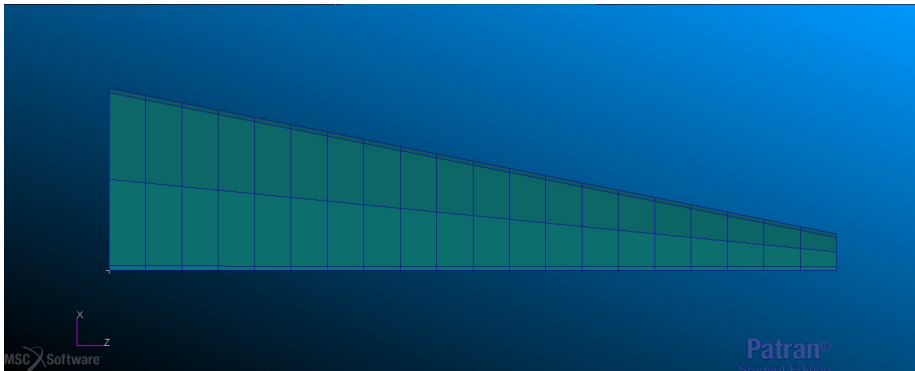
Figure 3.4.   (x,z)-plane view

The wing structure thus created is composed of 5 main groups, each of which presents different materials and thicknesses: the upper and lower skin panels, are made of a composite laminate; the ribs, a thicker structural part that is introduced to allow the application of concentrated loads; the spar caps, which are the connecting point between spar and panels; the stringers, which are distributed as shown in fig. 3.9, and the two front and rear spars which are made of aluminium alloy. In the table 3.1 are reported the thicknesses of the various parts that constitutes the wing and their material.
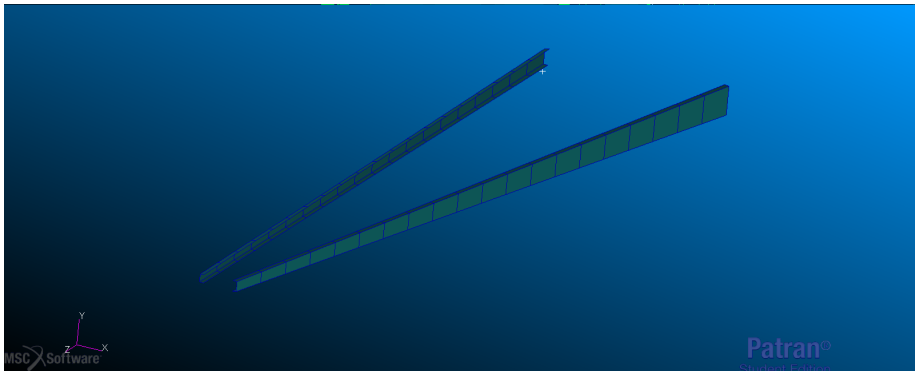
Figure 3.5.   Front and rear spars
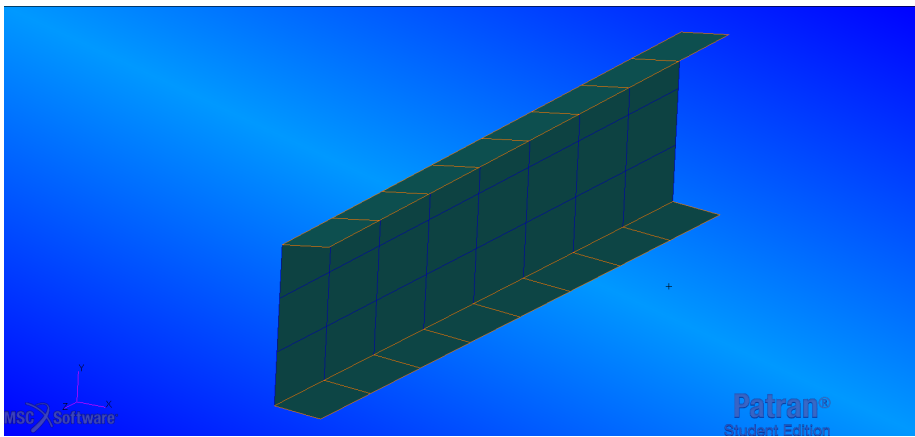
Figure 3.6.   Detail of spar and spar caps
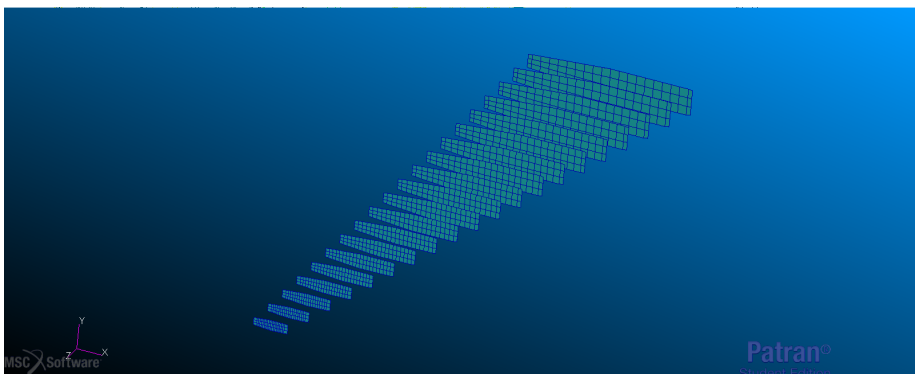
Figure 3.7.   Ribs along the model

21

Part	Thickness [mm]	material
Skin panels	8	Composite laminate
Spars	9	Aluminium alloy
Ribs	12	Aluminium alloy
Spar caps	14	Aluminium alloy
Stringers	tab 3.1	Aluminium alloy

Table 3.2.   Main characteristics on the structure's part

It is important to highlight that the values used for the aluminium alloy, as well as those which are shown below for the composite laminate, for the σ_r and the σ_y have been assumed considering the values of the various aluminium alloys, without however choose a particular one, and since the structure is not properly dimensioned, in the phase of control when it will be subjected to the gust loads, the maximum stresses values could be exceeded: this, as mentioned, is due to various factors such as the non-sizing of the structure parts or the fact that in this analysis the loads due to the weight of the fuel or of the structure itself are not taken into consideration. This also implies that deflections due to the loads will be excessive, but this will be explained later.

Aluminium alloy properties	Value
Young modulus (E)	73000 MPa
Shear modulus (G)	27000 MPa
Poisson's ratio (ν)	0.33
Density	2700 kg/m^3
Tensile ultimate σ_r	480 MPa
Yield strength σ_y	345 MPa

Table 3.3.   Aluminium alloy characteristics

A carbon-epoxy composite laminate made of 20 layers of carbon fiber in an epoxy resin matrix was used for the skin panels, and every layer has a thickness of 0.4 mm having that the whole panel is 8 mm, and whose lamination is obtained with the properties in table 3.1.
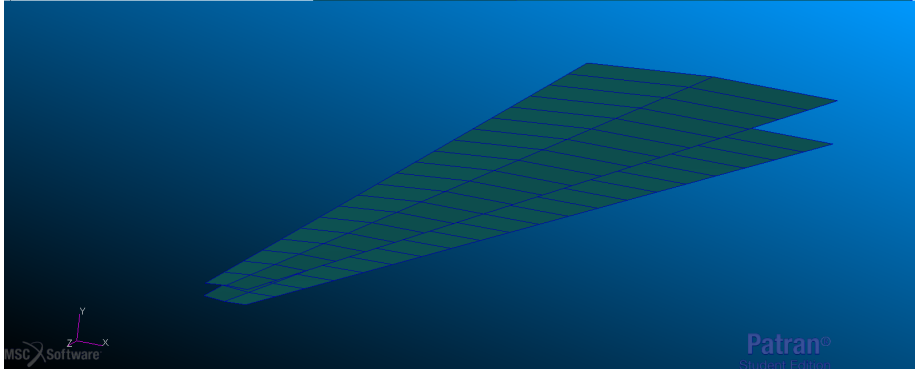
Figure 3.8.   Top and bottom skin panels in the model

Laminate properties	Value
Young modulus direction 1 (E_1)	$111000\,\mathrm{MPa}$
Young modulus direction 2 (E_2)	$8000\,\mathrm{MPa}$
Shear modulus $G_{12} = G_{13} = G_{23}$	$3000\,\mathrm{MPa}$
Poisson coefficient ν_{12}	0.33
Density	$1500\,\mathrm{kg/m^3}$
$[45\,/-45\,/\,0\,/\,0\,/\,90\,/\,0\,/\,0\,/-45\,/\,45\,/\,90]s$	

Table 3.4.   Composite laminate properties

As for the stringers, they were created using the beam property, as BAR3 elements, whose main values can be seen in the table 3.1; The use of the BAR3 elements, instead of the BAR2, is given by the fact that the latter is composed only by 2 nodes, one at each end of the element, defining a linear displacement variation along the element, versus a BAR3 element which has a quadratic displacement variation, even if it has a middle node. For this reason the BAR3 element was chosen because is more accurate in our case and fits better with the model's nodes. As can be seen from fig 3.10 we opted for Z-shaped stringers.

The connection of the beam elements was made using the existing mesh nodes, that from a rib to the next one, considering also those of the rib, corresponds to 5, having in this way the BAR3 elements between the two ribs, with a common joint node, and with the central node of each element that coincides with the pre-existent panel's mesh node. Moreover, their distribution along the wing span is made to avoid that the intermediate space between the various springers is neither too wide nor too narrow, as can be seen from the fig. 3.9. They are halved form the middle of the wing span, since the load from that point on is smaller so their presence could be

23
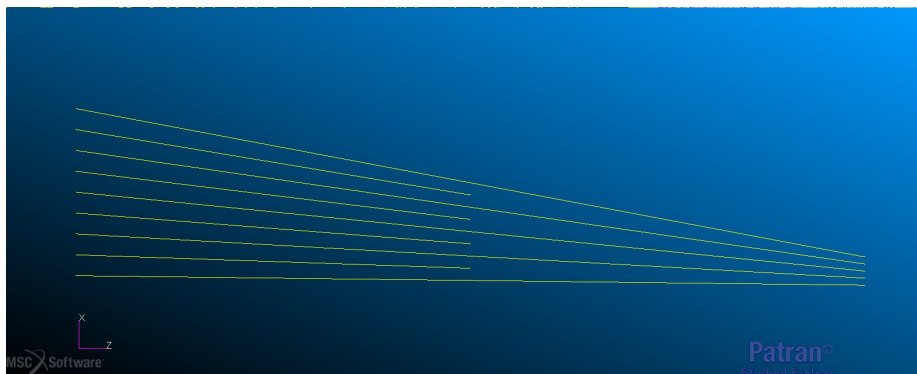
Figure 3.9.   Stringers deployment in the structure

superfluous for the purposes of the stiffness of the structure, contributing only to the increase of the weight.
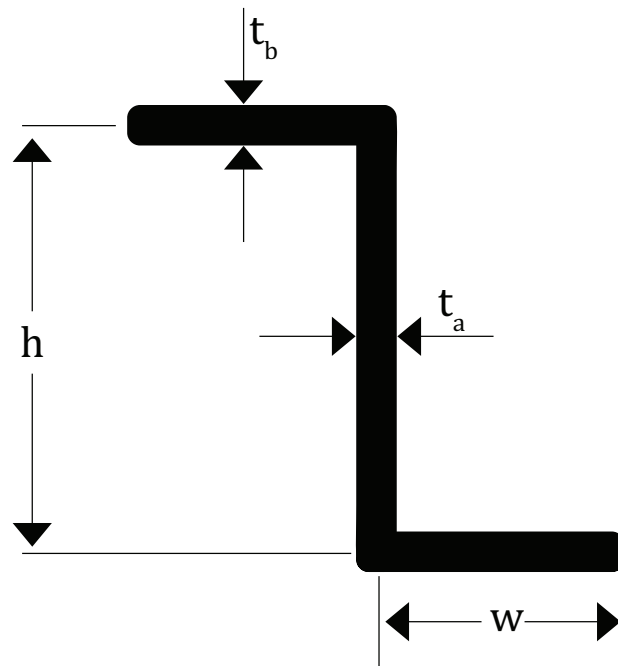
Figure 3.10.   Stringer section

Stringer section properties	Value [mm]
t_b	3
t_a	3
w	20
h	47

Table 3.5.   Stringer section properties
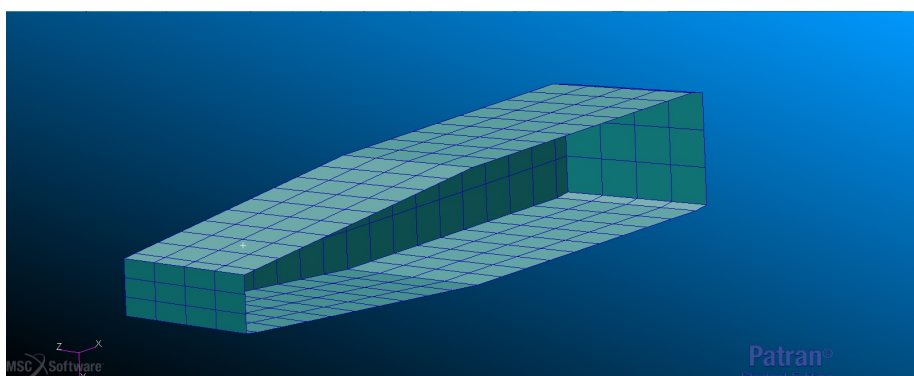
Figure 3.11.   Section model with various elements

3.1.1   Loads

The main purpose of the thesis is the reduction of the loads acting on the structure. Before to go any further, some of the adjustments used in the implementation of the loads in the model will be pointed out below. First of all it is essential to illustrate that two different types of loads were applied: the first type is constituted by concentrated loads, applying the force in some nodes of the structures, in particular in correspondence of the ribs, and a second set made by distributed loads, which are distributed along the upper and lower surfaces of the structure according to the specific distribution laws. The choice of applying the load in two different ways and in two different analysis, is due to the fact that when we are going to analyse the concentrated model. Being based on the representation of the structure as a succession of beams, is more convenient for the application of the loads to apply directly the concentrated ones instead of using the distributed; doing this is possible to avoid making a further step to discretize the distributed loads, in order to apply them on the nodes of the beam-like structure. In this way it is also possible to evaluate the correctness of the reconstruction of the concentrated model, applying the same loads to the two structures. The use of a distributed load instead aims to subject the structure to a more

truthful load, applying a pressure distributed along the upper and lower surfaces of the structure, which better simulates the aerodynamic forces to which the structure is subjected. The differences that characterize the two results will certainly be highlighted, both because the FEM elements will respond differently to the two types of loads, and because the distribution of pressures will be composed as the sum of a force and a moment.

For the shape of the distribution of forces acting on the wing, was chosen an elliptical shape

$$L = \frac{1}{2}\rho S V^2 C_L \tag{3.1}$$

where *rho* is the density of the air at the chosen flight altitude, S is the complete wing surface, V is the velocity of the flow that invests the profile, and C_L is the coefficient of lift of the profile. It is noted that the air density is obtained from the flight altitude $h = 6096$ [m] through the thermal gradient which influences the temperature of the atmosphere as its altitude changes, thus having a resulting density at a certain height given by

$$\rho = \rho_0 \left(\frac{T_0 - g \cdot z}{T_0} \right)^{4.256} \tag{3.2}$$

where ρ_0 represents the density of air at the sea level, with T_0 the standard sea level temperature of $288.15 K$, and with g the vertical thermal gradient that is $0.0065 \frac{K}{m}$. The lift coefficient is composed by a contribution due to the complete profile and its angle of incidence with respect to the flow direction that invests it, and a component due to the rotation of the aileron that changes the characteristics of the profile. Indicating with α the angle of incidence between the profile and the flow, and with δ the angle of rotation of the aileron, we have that

$$C_L = Cl_\alpha \cdot \alpha + Cl_\delta \cdot \delta \tag{3.3}$$

The equation 3.3 will be very important when we are going to apply the control, since it will be through the deflection of the aileron angle that the control will be carried out.

Referring to the equation 3.1 we have chosen an elliptic-type lift distribution, having therefore, in the z direction, that is the span-wise direction for the wing structure, the lift represented as

$$L(z) = \int_0^{b/2} L_0 \sqrt{1 - \left(\frac{z}{b/2}\right)^2} \qquad (3.4)$$

where $b/2$ is the wings span and the value L_0 is obtained knowing the total lift L and the value of the integral of the elliptical distribution $\sqrt{1 - \left(\frac{z}{b/2}\right)^2}$.
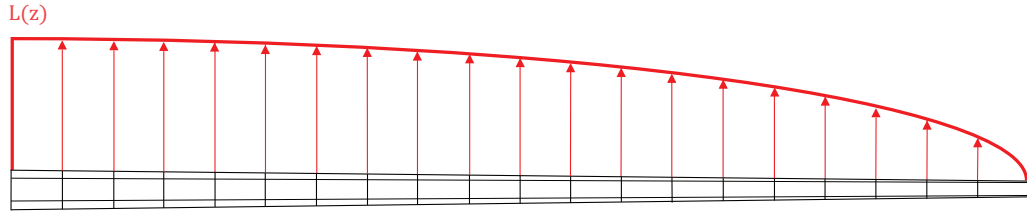
Figure 3.12.   Lift distribution on the model

The choice of the elliptical distribution for the lift was made because, according to the 3D aerodynamic theory, it is the shape that has the least induced drag and the greater aerodynamic efficiency, even if in this case the surface plan is trapezoidal, and therefore also the form of the lift should have this shape, given that the shape of the lift force around the profile

$$L(z) \propto \int_0^z c(z) \qquad (3.5)$$

which causes the shape of the surface to influence the distribution of lift. In the Prandtl finite wing theory, the aerodynamic forces are applied, on a profile, to the front quarter of the chord, but in this case the aerodynamic forces will be applied to $\frac{1}{3}c$: this is because in the case of distributed loads a triangular pressure distribution along the chord has been chosen. This means that in the comparison with the concentrated load, those will be applied on the center of gravity of the chord-wise pressure distribution, that correspond in this case to $\frac{1}{3}$. Moreover, it is not the purpose of this analysis to provide an aerodynamic analysis of the structure, but to evaluate

the reconstruction of the forces acting on it, for this reason approximations to the aerodynamic theory of the wing have been adopted, however trying to remain faithful to the real forces distribution, in order to obtain realistic results.

Concentrated

The analysis with concentrated loads requires an application point for the concentrated forces, since applying them on a single node of the model could lead to excessive and inaccurate deformations, thus distorting the structure response. For this reason the concentrated loads have been applied to the sections of the wingspan coinciding with the ribs, so as to better support the transverse loads, avoiding deformations that are not suitable for the panels. To apply those loads, MPC (Multi Point Constrains) elements of the RBE3 type were used, linked to the nodes that join the connecting elements between the panels and the ribs, in order to distribute the concentrated forces and moments between all the nodes, having a more accurate response.

Figure 3.13.   Application of the concentrated force from the lift distribution

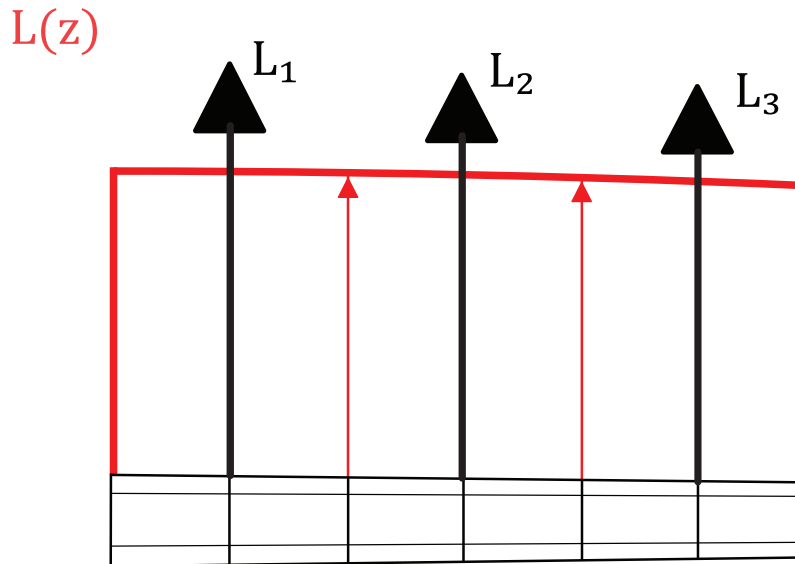For the calculation of the values of the concentrated forces, once the distribution of lift is obtained, as shown in eq.3.4, it has been divided into

10 parts, equally divided along the wingspan, and calculating the integral of the force distribution on each load section, the resultant force value have been applied as a concentrated force on the rib which it is located at the midpoint of the section, as in fig. 3.13.

The analysis with the concentrated forces allow us to use these loads as forces applied to the nodes of the concentrated model, being able in this way to make a comparison between the two models, verifying their accuracy.

Distributed

The concentrated loads analysis case is used to better compare the complete structure and the concentrated one. But an analysis of the structure subject to distributed loads is however carried out, as they better represent the real forces to which the structure will be subjected. It's now illustrated the characteristics of the forces that have been used to load the structure. Instead of distributed forces, it was decided to apply distributed pressures, on the upper and lower surfaces of the structure, because the lift is generated by a difference of pressure between the upper and the lower surfaces of the profile, with an overpressure on the lower one accompanied by a depression on the upper one. This create a pressure difference that generate the lift, and this reason lead to apply a pressure load cause is more realistic. Following this consideration it is logical to think to distribute the pressure load among the two upper and lower surfaces to better simulate the lift, having so a pressure contribution acting on the two surfaces. In addition to consider a dependence of the lift forces along the wingspan, which follows an elliptical shape as reported by the equation 3.4, instead of applying a pressure with such distribution on a line corresponding to a quarter of the chord from the leading edge, it was chosen to provide a chord-wise pressure distribution, choosing a triangular shape distribution. This distribution has a maximum value at the point corresponding to the front spar, linearly decreasing up to the null value at the rear spar.
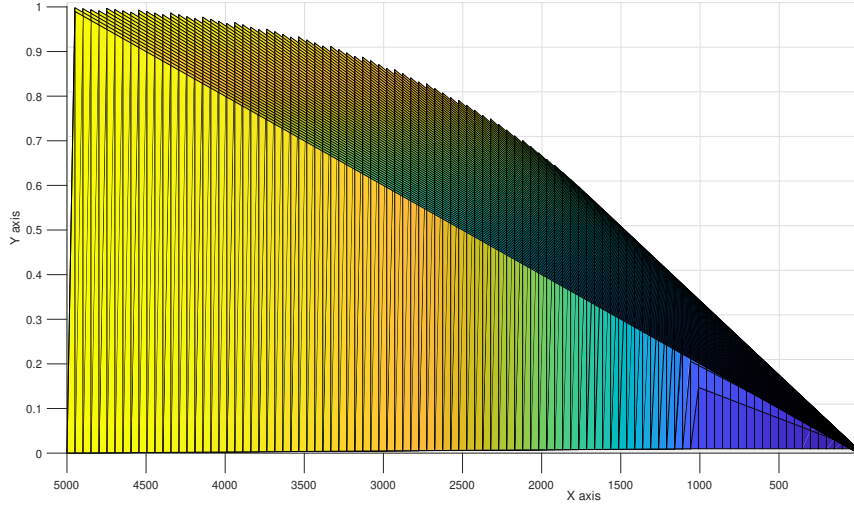
Figure 3.14.   Chord-wise pressure distribution

Considering therefore the ramp distribution along the chord, considering the distribution as in the eq. 3.4, the pressure distribution applied to surfaces is obtained as

$$L(x,z) = L_{0_{x,z}} \sqrt{1 - \left(\frac{z}{b/2}\right)^2} \cdot x \left(c_r - \frac{c_r - c_t}{b/2 \cdot z}\right) \tag{3.6}$$

where c_r e c_t are the values of the chord at the root and at the tip section respectively, and $L_{0_{x,z}}$ it's constant value that is obtained, in a similar way to what was done for the distribution of concentrated forces, from the equation 3.1. Note well that the values of the constant L_0 and $L_{0_{x,z}}$ are different values, because in the case of concentrated loads it was used to relate the integral of the distribution $\int_0^{b/2} \sqrt{1 - \left(\frac{z}{b/2}\right)^2}$ to the value of the lift L referring to the 3.1, while in the case of $L_{0_{x,z}}$ it relates to the value of the double integral $\int_0^{b/2} \int_0^{c(z)} \sqrt{1 - \left(\frac{z}{b/2}\right)^2} \cdot x \left(c_r - \frac{c_r - c_t}{b/2 \cdot z}\right)$.
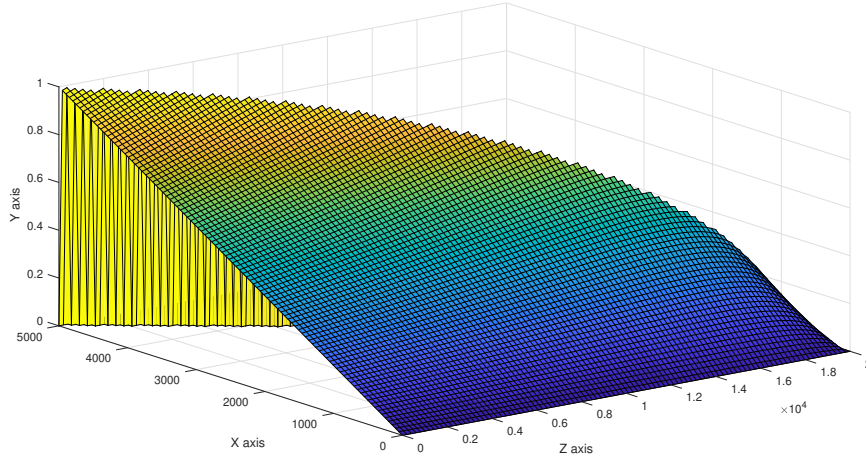
Figure 3.15.   Total pressure distribution

3.2   Control Model

This part of the chapter focuses on how the finite element model is reduced to a simplified beam-like model. Since there are different techniques, such as static condensations of the mass and stiffness matrix, in this case we have opted for the creation of an aircraft simplified beam finite element model, also known as stick model, which is commonly used in the design of civilian aircraft or also in multidisciplinary design optimization (MDO). An accurate prediction of the deformations due to twists and bends in the structure of the aircraft depends on the accuracy with which the stiffness characteristics are collected and reconstructed from the model. In particular, the process for the generation of a stick model is based on the extraction of the stiffness properties of the main structure and applying it to a set of beams which displaced along the elastic axis of the structure. The possibility of having a simplified structural model of the entire structure of the aircraft is very important in the aeronautical field. Having the deformations of the aircraft's structure during the flight is important also from the point of view of the aerodynamic performances, since that the aerodynamic loads can be used for the preliminary dimensioning of the structure. The finite element 3D model is usually used mainly after that the structural details are obtained, for this reason is used for verification, validation and optimization from a structural point of view. This gives that a simplified FEM beam model is more useful in the preliminary studies because is enough accurate and is

cheaper to develop from both the financial and the computational point. The difficulty in constructing such a model is that it's needed to be able to develop it sufficiently simple but at the same time quite sophisticated and accurate enough to predict the dynamic trend of the structure. Taking as a guideline the method used in [12], is explained how the beam model has been developed.
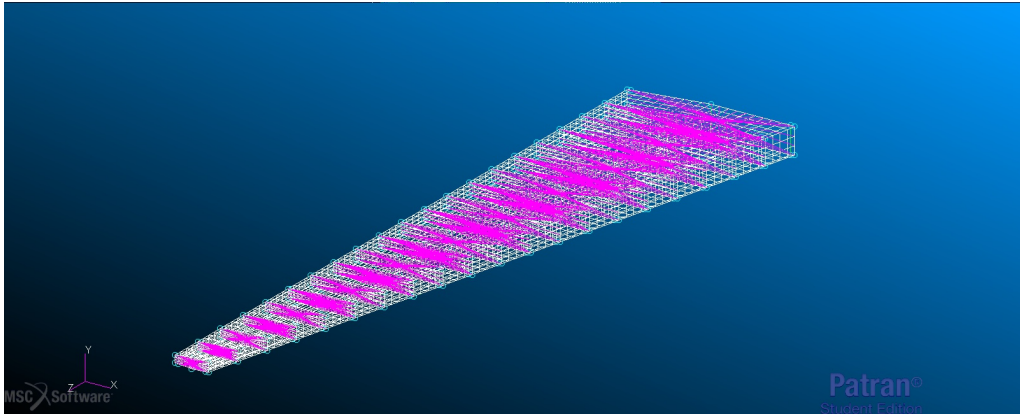
Figure 3.16.   Complete detailed FEM model

3.2.1   Stiffness

The analysis for the reconstruction of the stiffness of the beam, starting from the complete FEM model, consists of a process divided into 3 phases:

- First of all the axes for referencing the beam and the nodes of the beam elements in the complete FEM are defined;

- Flexibility matrices are determined numerically, through the behaviour of the complete FEM submitted to a small number of static load cases;

- For each element are calculated a set of 13 physical parameters necessary to define by rigidity of the beam element.

As far as the first two steps are concerned, this is nothing more than the result of Malcolm and Liard process for the BPE [9], while the third step create a small number of independent physical parameters. This analysis

assume linear behaviours of the structure, with small wing deflections and rotations.

In the figure 3.16 it's exposed the complete model, and in the figure 3.17 the associated beam structure is represented on a $x - z$ plan view. The reference axis for the beam model, correspond to the line that link all the nodes of the beam elements from the root section to the tip one. The definition for the reference axis of the beam has not particular guidances, except that it must be continuous and aligned with the structure of the wing. For each section a xyz local coordinate system (LCS) is defined as shown below, highlighted in red, where the z axis extends from the beam node of the root section to that of the tip section.
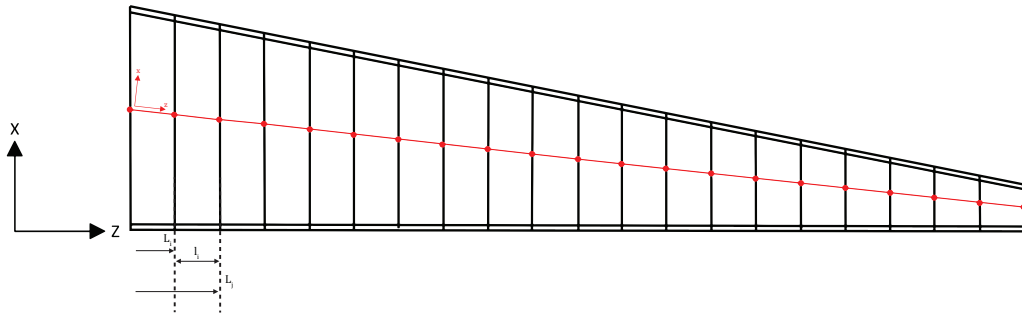
Figure 3.17.   Representation of the concentrated beam model compared to the complete one in the $x - z$ plan

Referring to the figure 3.16 of the complete structure, it has been divided in different sections, corresponding to them bounded between two consecutive ribs, with the root section fixed through the constraints. It is advisable to make the sections coincide with the beam element so that the structural stiffness, provided by ribs and stringers, allows greater accuracy in the results. But also choosing sections that do not correspond to these areas should not be considered wrong. Moreover, as mentioned previously, there are no contraindications on the choice of the beam reference axis, which for example may not be perpendicular to the selected sections. Considering now each box section, an element RBE3 is applied to the nodes of that section, connecting them with to the node corresponding to the section axis. By doing this the node will be dependent on the displacement of all the nodes in the section. The dependant node corresponds to the node on the shear center of that section. There are no contraindications on the number of nodes of the section to be included, but it is suggested to take those corresponding to the junctions between the various structural parts, such as skin-ribs or skin-spar. In the figure 3.18 there is an example of the MPC

link between the dependant done (the one in the center) and the nodes of the section.
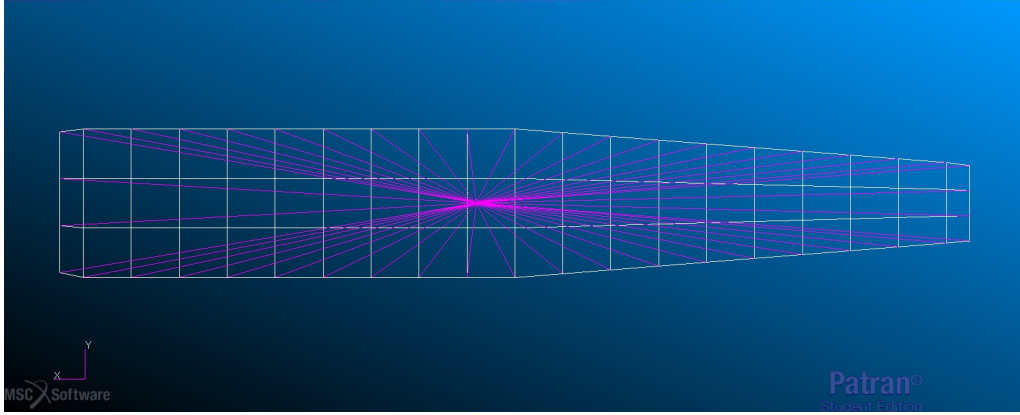
Figure 3.18.   Side view of the structure section with the MPC connections

It is suggested to include, as node's section, the ones that are not included inside the rib, but only the one on the structural junctions, as the ones with the panels. This because, applying the loads, there could be distorted deformations on the core of the rib.

The choice of the RBE3 element instead of the RBE2 element is motivated by the fact that although it may be more appropriate to use RBE2 elements for structures formed by spar-ribs structures, but since our panels are made of composite layers, it is no longer advised, since introduces a stiffness that does not represent the real one of the structure. This because this element introduce constraints conditions between the dependent node and the independent ones, which fix the distance between them and the dependent one, thus introducing a much greater resistance in that degree of freedom.

The properties of the equivalent beam are extracted from the various boxes through a static analysis, which follows the following expression

$$\{F\} = [K]\{u\} \rightarrow [K]^{-1}\{F\} = \{u\} \rightarrow [FF]\{F\} = \{u\} \qquad (3.7)$$

where $\{F\}$ it is the vector containing the forces and moments, $\{u\}$ is the displacements vector, $[K]$ is the stiffness matrix and $[FF]$ is the flexibility

matrix. It can also be noted that by applying forces and unit moments it is possible to derive the flexibility matrix as the following equation shows:

$$\begin{bmatrix} u_1 & \dots & \dots & \dots & \dots & \dots \\ u_2 & \dots & \dots & \dots & \dots & \dots \\ u_3 & \dots & \dots & \dots & \dots & \dots \\ u_4 & \dots & \dots & \dots & \dots & \dots \\ u_5 & \dots & \dots & \dots & \dots & \dots \\ u_6 & \dots & \dots & \dots & \dots & \dots \end{bmatrix} \begin{Bmatrix} 1 \\ 0 \\ 0 \\ 0 \\ 0 \\ 0 \end{Bmatrix} = \begin{Bmatrix} u_1 \\ u_2 \\ u_3 \\ u_4 \\ u_5 \\ u_6 \end{Bmatrix} \tag{3.8}$$

In eq.3.8 it's showed that applying an unit load is it possible to calculate the components of the flexibility matrix due to that load as the displacement vector $u_{1rightarrow6}$. Each section, corresponding to the MPC, has its own flexibility matrix, whose dimension is $n \times n$, with n number of degree of freedom, and is obtained aligning the various displacement vectors due to the unit load, composing in this way, the flexibility matrix. It is important, in order to increase the accuracy of the reconstruction, to apply the unit loads separately, so to analyse the response of the section for each load.
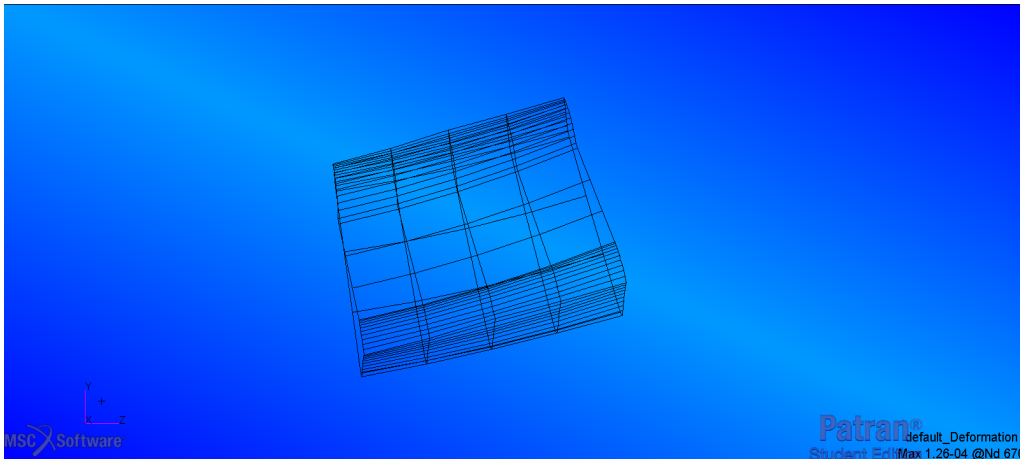
Figure 3.19. $z - y$ plan view of the structure section deformation due to an unit load along y axis

Following this procedure, are derived the flexibility matrices at the stations j and i, or $[FF]_j$ and $[FF]_i$. It should be noted that since the loads are very small, the flexibility matrices can result in very small values, even close to zero, which could lead to results which do not correspond to the true properties of the section.
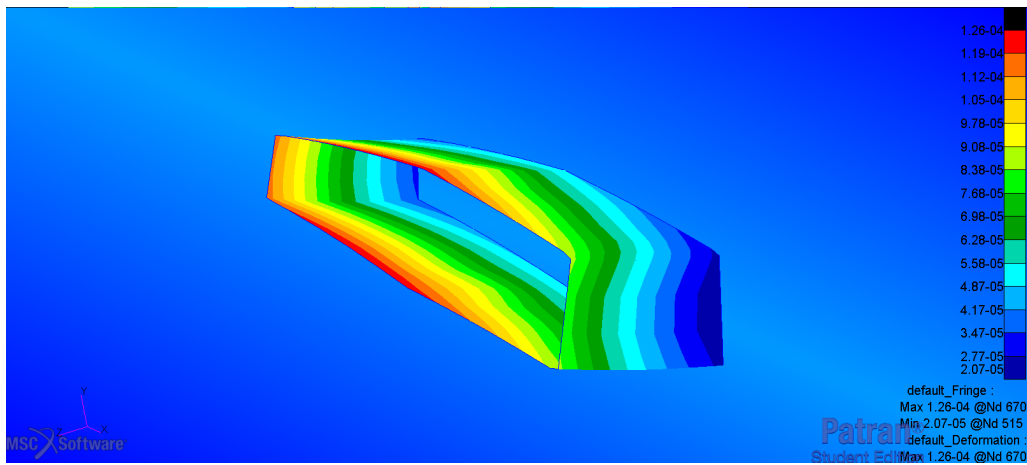
Figure 3.20. Structure section deformation due to an unit load along y axis

Considering then l_i the distance between the various nodes of the beam in the global reference system, fig. 3.21

$$l_i = L_j - L_i \tag{3.9}$$
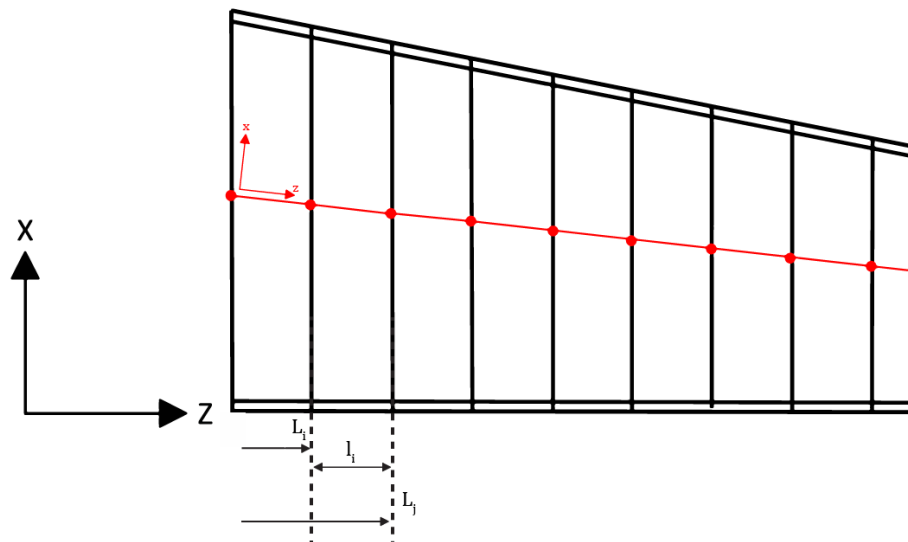
Figure 3.21. Distance between the various sections on the global reference system

the flexibility matrix of the entire j-th section $[ff]_j$ can be calculated as

$$[ff]_j = \frac{[FF]_j - [FF]_i}{l_i} \tag{3.10}$$

from which I can then derive the stiffness matrix associated at each section, which corresponds to that of the equivalent beam

$$[kk]_j = [ff]_j^{-1} \rightarrow \{F\} = [kk]\{u\} \tag{3.11}$$

Once the stiffness matrix of the beam element has been found, it is now necessary to compensate the offset of the elastic axis of the beam element and of its shear center. This offset is caused by the non-alignment between the reference axes of the complete system and the reference axes of the various beam elements, reported in fig. 3.17. In order to match the two reference systems, we need to introduce rotation matrices that rotate the axes from the global reference system to the local one, of the element. Since in our case, the structure is symmetrical with respect to a plane parallel to the $x - z$ one, a rotation of the y axis is not necessary but for completeness it will be considered within the following equations.

Taking into consideration the flexibility matrix of the $j - th$ element $[ff]_j$, and naming with γ_p^q the angles relative to the p axis in the rotation $q =',',''','''$. The $[R]$ rotation matrix is created

$$[R] = \begin{bmatrix} T & 0 \\ 0 & T \end{bmatrix} \tag{3.12}$$

where $[T^q]$ is

$$T' = \begin{bmatrix} cos(\gamma_z) & -sin(\gamma_z) & 0 \\ sin(\gamma_z) & cos(\gamma_z) & 0 \\ 0 & 0 & 1 \end{bmatrix} \; for \; i = z \tag{3.13}$$

$$T'' = \begin{bmatrix} cos(\gamma_y) & 0 & sin(\gamma_y) \\ 0 & 1 & 0 \\ -sin(\gamma_y) & 0 & cos(\gamma_y) \end{bmatrix} \; for \; i = y \tag{3.14}$$

37

$$T''' = \begin{bmatrix} 1 & 0 & 0 \\ 0 & cos(\gamma_x) & -sin(\gamma_x) \\ 0 & sin(\gamma_x) & cos(\gamma_x) \end{bmatrix} \; for \; i = x \qquad (3.15)$$

In this way, the rotation matrices are obtained to perform the rotations through which it is possible to pass from a reference system xyz to a $x'y'z'$. Instead of using these rotational matrices, you can use those relative to Euler's angles, respectively referred to as the angle of nutation, angle of rotation, and angle of precession. Assuming therefore that we want to switch from our system xyz to that $x'y'z'$ we have the definition of the 3 angles as

- θ as angle between the axis z' and the axis z

- ϕ as an angle between the axis x' and the line of intersection between the $x'y'$ plane and the xy plane also called *line of nodes*

- ψ angle between the line of the nodes and the axis x

Following these 3 angles we are able to make a rotation following $\theta,\phi\psi$ to overlap the systems xyz e $x'y'z'$ through, respectively

1. counterclockwise rotation of ψ angle around the z axis

2. counterclockwise rotation of θ angle around the node line, which now coincides with x

3. counterclockwise rotation of ϕ around the z' axis.

similarly to how indicated above, these rotations can be expressed in terms of rotation matrices, with the matrices associated with the 1,2,3 rotations as

$$T_1 = \begin{bmatrix} cos(\psi) & -sin(\psi) & 0 \\ sin(\psi) & cos(\psi) & 0 \\ 0 & 0 & 1 \end{bmatrix} \qquad (3.16)$$

$$T_2 = \begin{bmatrix} 1 & 0 & 0 \\ 0 & cos(\theta) & -sin(\theta) \\ 0 & sin(\theta) & cos(\theta) \end{bmatrix} \qquad (3.17)$$

$$T_3 = \begin{bmatrix} cos(\phi) & -sin(\phi) & 0 \\ sin(\phi) & cos(\phi) & 0 \\ 0 & 0 & 1 \end{bmatrix} \tag{3.18}$$

obtaining a complete rotation matrix from them $\mathcal{T} = T_1 T_2 T_3$ which looks like

$$\mathcal{T} = [(\cdot)_1 \, (\cdot)_2 \, (\cdot)_3] \tag{3.19}$$

with

$$(\cdot)_1 = \begin{pmatrix} cos(\psi)cos(\phi) - sin(\psi)cos(\theta)sin(\phi) \\ sin(\psi)cos(\phi) + cos(\psi)cos(\theta)sin(\phi) \\ sin(\theta)sin(\phi) \end{pmatrix} \tag{3.20}$$

$$(\cdot)_2 = \begin{pmatrix} -sin(\phi)cos(\psi) - sin(\psi)cos(\theta)cos(\phi) \\ -sin(\psi)sin(\phi) + cos(\psi)cos(\theta)cos(\phi) \\ sin(\theta)cos(\phi) \end{pmatrix} \tag{3.21}$$

$$(\cdot)_3 = \begin{pmatrix} sin(\psi)sin(\theta) \\ sin(\theta)cos(\psi) \\ cos(\theta) \end{pmatrix} \tag{3.22}$$

having therefore that the matrix of flexibility of the elements in the global system becomes

$$\left[\overline{ff_j}\right] = [R][ff_j][R]^T = \begin{bmatrix} \mathcal{T} & 0 \\ 0 & \mathcal{T} \end{bmatrix} [ff_j] \begin{bmatrix} \mathcal{T} & 0 \\ 0 & \mathcal{T} \end{bmatrix}^T \tag{3.23}$$

3.2.2   Mass

For the mass matrix reconstruction, a "lumped" masses and inertias approach is used, calculating them at the beam nodes approximating the mass properties of the complete FEM along the wing span. As before, the FEM model is divided into various sections associated with the nodes of the beam elements, thus calculating the mass and inertia properties. For each group

of elements an equivalent mass m_s, a CG center of gravity and an inertia with respect to the beam reference system are determined as:

$$m_s = \sum_{i=1}^{n} m_i \tag{3.24}$$

$$X_{CG} = \sum_{i=1}^{n} \frac{X_i m_i}{m_s} \tag{3.25}$$

$$Y_{CG} = \sum_{i=1}^{n} \frac{Y_i m_i}{m_s} \tag{3.26}$$

$$Z_{CG} = \sum_{i=1}^{n} \frac{Z_i m_i}{m_s} \tag{3.27}$$

$$I_{XX} = \sum_{i=1}^{n} m_i \left(Y_i^2 + Z_i^2 \right) \tag{3.28}$$

$$I_{YY} = \sum_{i=1}^{n} m_i \left(X_i^2 + Z_i^2 \right) \tag{3.29}$$

$$I_{ZZ} = \sum_{i=1}^{n} m_i \left(Y_i^2 + X_i^2 \right) \tag{3.30}$$
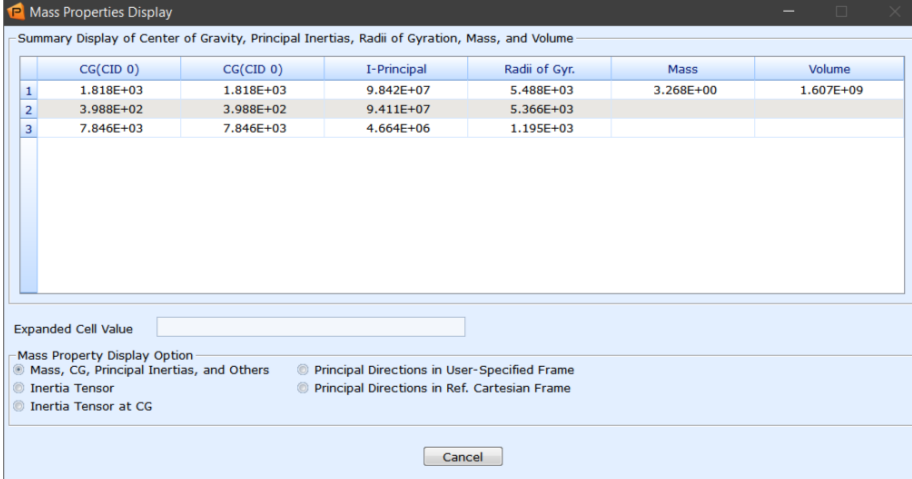
$$I_{XY} = \sum_{i=1}^{n} m_i X_i Y_i \tag{3.31}$$

$$I_{XZ} = \sum_{i=1}^{n} m_i X_i Z_i \tag{3.32}$$

$$I_{YZ} = \sum_{i=1}^{n} m_i Y_i Z_i \tag{3.33}$$

where m_i,X_i,Y_i and Z_i are the mass of element i and the distance of its centroid from the beam node. So the 6×6 symmetric mass matrix $[M]$ at the beam node may be then be determined from

$$
\begin{bmatrix} M \end{bmatrix} = \begin{bmatrix} m_s & & & & & \\ 0 & m_s & & sym. & & \\ 0 & 0 & m_s & & & \\ 0 & 0 & 0 & I_{XX} & & \\ 0 & 0 & 0 & -I_{XY} & I_{YY} & \\ 0 & 0 & 0 & -I_{XZ} & -I_{YZ} & I_{ZZ} \end{bmatrix} \tag{3.34}
$$

Alternatively, it's possible to use the tool contained in PATRAN, *Mass Properties*, so that the properties of the detailed FEM model can be found. For the calculation of the mass properties, as reported in tab. 3.2.2, this tool was used. The software provides to obtain the mass, the position of the center of gravity and the inertia tensor of an area of the model. Therefore it is possible to select the mass properties of the sections created for the reduction. Once these properties are obtained they can be modelled as concentrated masses placed in the beam nodes with CONM2 elements of NASTRAN. This element in particular allows to shape the inertia tensor, as well as the position of the center of gravity, with an offset with respect to where the element is positioned. In this way the masses are well defined and all the properties of a possible reduced model are equal to those of the detailed one [8].

Figure 3.22.   Mass properties

Section	Mass [ton]	I_{XX} [ton · mm²]	I_{YY} [ton · mm²]	I_{ZZ} [ton · mm²]	I_{XY} [ton · mm²]	I_{XZ} [ton · mm²]	I_{ZY} [ton · mm²]
1	$2.773E-01$	$5.358E+04$	$7.114E+05$	$7.033E+05$	$1.129E+03$	$1.252E+02$	$9.660E+01$
2	$2.639E-01$	$4.985E+04$	$6.291E+05$	$6.201E+05$	$1.006E+03$	$3.257E+02$	$9.151E+01$
3	$2.508E-01$	$4.630E+04$	$5.538E+05$	$5.441E+05$	$8.938E+02$	$5.032E+02$	$8.646E+01$
4	$2.380E-01$	$4.292E+04$	$4.853E+05$	$4.750E+05$	$7.908E+02$	$6.581E+02$	$8.144E+01$
5	$2.255E-01$	$3.972E+04$	$4.231E+05$	$4.124E+05$	$6.967E+02$	$7.911E+02$	$7.647E+01$
6	$2.132E-01$	$3.669E+04$	$3.668E+05$	$3.558E+05$	$6.111E+02$	$9.029E+02$	$7.156E+01$
7	$2.012E-01$	$3.381E+04$	$3.161E+05$	$3.049E+05$	$5.333E+02$	$9.941E+02$	$6.671E+01$
8	$1.895E-01$	$3.109E+04$	$2.707E+05$	$2.594E+05$	$4.628E+02$	$1.066E+03$	$6.191E+01$
9	$1.781E-01$	$2.851E+04$	$2.301E+05$	$2.189E+05$	$3.993E+02$	$1.118E+03$	$5.719E+01$
10	$1.669E-01$	$2.607E+04$	$1.941E+05$	$1.830E+05$	$3.421E+02$	$1.152E+03$	$5.255E+01$
11	$1.561E-01$	$2.376E+04$	$1.623E+05$	$1.514E+05$	$2.909E+02$	$1.169E+03$	$4.800E+01$
12	$1.392E-01$	$2.065E+04$	$1.311E+05$	$1.208E+05$	$1.555E+02$	$1.204E+03$	$5.584E+01$
13	$1.293E-01$	$1.867E+04$	$1.076E+05$	$9.771E+04$	$2.058E+02$	$1.139E+03$	$4.068E+01$
14	$1.192E-01$	$1.677E+04$	$8.696E+04$	$7.754E+04$	$1.701E+02$	$1.104E+03$	$3.639E+01$
15	$1.095E-01$	$1.499E+04$	$6.932E+04$	$6.042E+04$	$1.388E+02$	$1.056E+03$	$3.222E+01$
16	$9.996E-02$	$1.331E+04$	$5.441E+04$	$4.608E+04$	$1.113E+02$	$9.970E+02$	$2.819E+01$
17	$9.075E-02$	$1.174E+04$	$4.195E+04$	$3.425E+04$	$8.751E+01$	$9.282E+02$	$2.430E+01$
18	$8.182E-02$	$1.026E+04$	$3.170E+04$	$2.465E+04$	$6.700E+01$	$8.512E+02$	$2.057E+01$
19	$7.316E-02$	$8.879E+03$	$2.341E+04$	$1.705E+04$	$4.952E+01$	$7.675E+02$	$1.702E+01$
20	$6.478E-02$	$7.588E+03$	$1.684E+04$	$1.118E+04$	$3.479E+01$	$6.787E+02$	$1.366E+01$

Table 3.6.   Mass properties

3.2.3   Damping

The estimation of damping in structures made up of different materials still remains one of the biggest and most extensive challenges, also because the concept of damping within a structural system can have different meanings according to different branches of study. Damping is the physical phenomenon by which mechanical energy is dissipated in dynamic systems (usually by transforming it into internal thermal energy), and a good understanding of the damping within a dynamic system is very important for the use, analysis and test of the system. We can divide the damping of the dynamic systems into 3 main contributions:

- Internal damping of the material, generated by the dissipation of mechanical energy inside the material due to microscopic and macroscopic processes;

- Structural damping, caused by the dissipation of mechanical energy resulting from the relative movements of the various mechanical components of the structure, which has contact points, junctions or supports;

- Fluid damping derives from the dissipation of mechanical energy due to drag forces associated with the dynamic interaction between a mechanical system and its components within a fluid.

The damping can be represented by different parameters and models, for this reason before trying to measure it within a system, we must decide a representation, through a certain model, that can describe the characteristics and nature of the dissipation of mechanical energy in the system. In general, damping is usually studied in two different ways: or through time-response or frequency-response methods, with the main difference, between the two methods, that in the first case it consists of a recording of the system's time response to measure the damping, while the latter is based on a recording based on the response in frequency.

Damping measurement

To better understand the damping that afflicts the structure, we take as an example the vibrational model of a cantilever beam, reporting the consideration taken in [16], which presents deformations due to bending with displacement measured along the y axis which satisfy the following eq

$$\frac{\partial^4 y}{\partial x^4} + \frac{\rho A}{EI} \cdot \frac{\partial^2 y}{\partial x^2} = 0 \tag{3.35}$$

where ρ is the density of the beam material, A is the cross section area of the beam, E is Young's modulus, and I is the cross section inertia of the beam. The equation can be solved as follows:

$$y(x,t) = \left[A cos\sqrt{\frac{\omega_n}{\sigma}}x + B sin\sqrt{\frac{\omega_n}{\sigma}}x + C cohs\sqrt{\frac{\omega_n}{\sigma}}x \right.$$

$$\left. + D sinh\sqrt{\frac{\omega_n}{\sigma}}x \right] \cdot sin(\omega_n t + \phi) \tag{3.36}$$

with

$$\sigma^2 = \frac{EI}{\rho A} \tag{3.37}$$

where ω_n is the $n - th$ natural angular frequency of vibration.

It is possible to solve the eq. 3.36 through the boundary conditions, depending on the model under analysis. When the conditions are such that there are small deformations, the behaviour of the first vibrating mode of a cantilever beam can be approximated to the behaviour of a system with one degree of freedom mass-string-damper, whose well-known equation describes vibration, as a linear system is

$$\ddot{x} + 2\zeta\omega\dot{x} + \omega^2 x = 0 \tag{3.38}$$

with the resonant frequency equal to $\omega = \sqrt{k/m}$ from which the damping ratio

$$\zeta = \frac{c}{2\sqrt{km}} = \frac{c}{2m\omega} \tag{3.39}$$
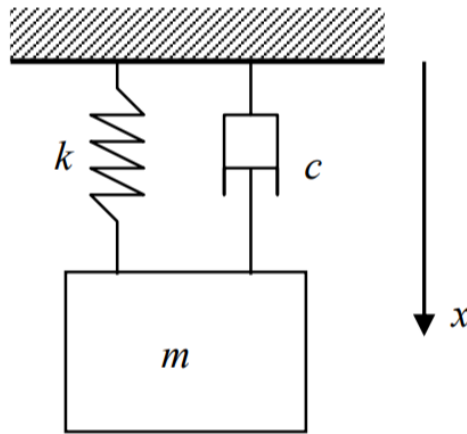
Figure 3.23.   Linear model

where k is the stiffness, c is the damping coefficient and m is the mass; the general solution of the equation can be written as

$$x(t) = A \cdot e^{-\zeta \omega t} \cdot cos(\omega \sqrt{1 - \zeta^2} \cdot t + \phi) \tag{3.40}$$

Usually in the methods used to measure the damping coefficient are based on the determination of the parameters ζ and ω.

It is possible to introduce the damping factor through the equivalent damping of Rayleigh, in fact, having the free vibration equation of a structure written as

$$m\ddot{x} + c\dot{x} + kx = 0 \tag{3.41}$$

where x it is a vector representing the displacement of each element of the structure. The Rayleigh's theory assumes that the damping matrix c is a function of mass and stiffness matrices that can be linearized with α and β as constants that multiply the matrices of mass m and stiffness k :

$$c = \alpha m + \beta k \tag{3.42}$$

Considering the mathematical theory of matrices, the same orthogonal transformation that allows to diagonalize m and k allows to diagonalize c. Is it possible in this way to write the equivalent expression:

$$M\ddot{\delta} + C\dot{\delta} + K\delta = 0 \tag{3.43}$$

where M, C and K are the diagonalized matrices, for a set of coordinates δ. So we can write, for each mode of vibration, an equation of the form:

$$M_{ii}\ddot{\delta}_i + C_{ii}\dot{\delta}_i + K_{ii}\delta_{ii} = 0 \tag{3.44}$$

that can be written as

$$\ddot{\delta}_i + 2\zeta\omega_i\dot{\delta}_i + \omega i\delta_{ii} = 0 \tag{3.45}$$

where ω_i and ζ_i are the resonance angular frequency and damping ratio of the $i-th$ mode. Since that the damping ratio for each mode, from 3.44 and 3.45 satisfies

$$2\zeta_i\omega_i = \frac{C_{ii}}{M_{ii}} \tag{3.46}$$

we can write as follow

$$\zeta_i = \frac{\alpha M_{ii} + \beta K_{ii}}{2\sqrt{K_{ii}M_{ii}}} = \frac{\alpha}{2\omega_i} + \frac{\beta\omega_i}{2} \tag{3.47}$$

More details about Rayleigh's model [18] of damping can be found in Newland (1989) [15] or Caughey and O'Kelly (1965) [13]. In almost all structural problems, the resonance frequencies are relatively high, so the

damping component related to the mass (the term involving α) is negligible. Therefore:

$$\zeta = \frac{\beta \omega_i}{2} \tag{3.48}$$

One of the methods that can be used to estimate the damping value is based on the magnitude of the frequency response function curve [11]. A bandwidth $\Delta \omega$ is defined as the depth of the frequency response magnitude when the magnitude is $\dfrac{1}{\sqrt{2}}$ of the peak value.. So the damping ratio can be determined by the bandwidth using the equation

$$\zeta = \frac{1}{2} \frac{\Delta \omega}{\omega_n} \tag{3.49}$$
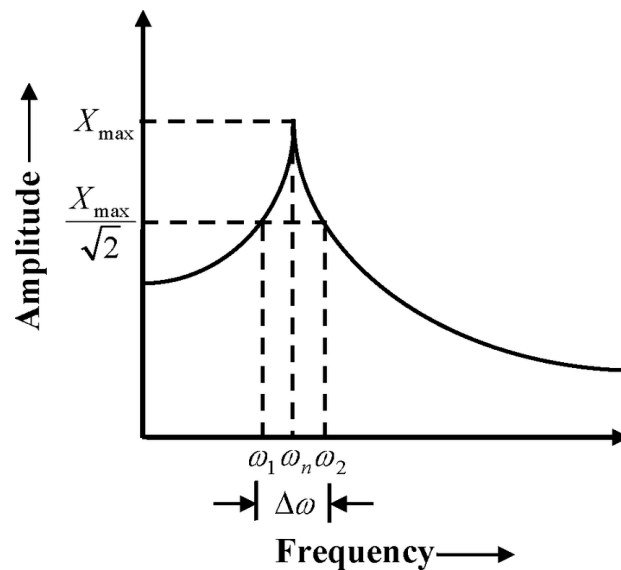
Figure 3.24.   Half power widthband method

In the case of an underdamped system, i.e. with $\zeta < 1$ we can write the solution of the differential equation of our system as

$$x(t) = C_1 e^{(-\zeta + i\sqrt{1-\zeta^2})\omega_n t} + C_2 e^{(-\zeta - i\sqrt{1-\zeta^2})\omega_n t} =$$
$$= e^{-\zeta\omega_n t}\left\{C_1 e^{i\sqrt{1-\zeta^2}} + C_2 e^{i\sqrt{1-\zeta^2}}\right\} \quad (3.50)$$

that we can lead back to the form

$$x(t) = X_0 e^{-\zeta\omega_n t}cos(\sqrt{1-\zeta^2}\omega_n t - \phi_0) \quad (3.51)$$

where

$$X_0 = \frac{\sqrt{x_0^2\omega_n^2 + \dot{x}_0^2 + 2x_0\dot{x}_0^2\zeta\omega_n}}{\sqrt{1-\zeta^2}\omega_n} \quad (3.52)$$

$$\phi_0 = tan^{-1}\left(\frac{\dot{x}_0^2 + \zeta\omega_n x_0}{x_0\omega_n\sqrt{1-\zeta^2}}\right) \quad (3.53)$$

Figure 3.25.   Response of the under-damped system with logarithmic decrease

As can be seen from the figure 3.25 we see how in the presence of damping the amplitude of the response decreases over time according to a logarithmic

48

law, and one can find a correlation between the damping that acts and the relationship between two successive oscillation peaks, in fact
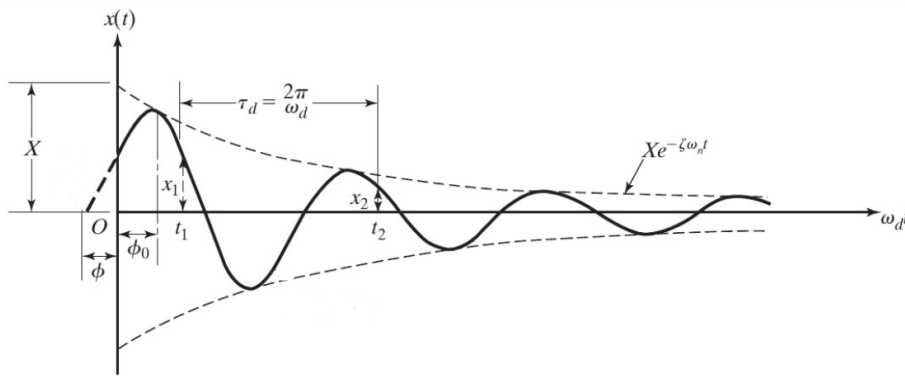
$$\frac{x_1}{x_2} = \frac{X_0 e^{-\zeta \omega_n t_1} cos(\sqrt{1 - \zeta^2} \omega_n t_1 - \phi_0)}{X_0 e^{-\zeta \omega_n t_2} cos(\sqrt{1 - \zeta^2} \omega_n t_2 - \phi_0)} \tag{3.54}$$

and given that

$$t_2 = t_1 + \tau_d \tag{3.55}$$

and

$$\tau_d = 2\pi/\omega_d \tag{3.56}$$

with τ_d oscillation period, and $\omega_d = \sqrt{1 - \zeta^2}$ the damped pulsation of the oscillation, we can write that

$$cos(\omega_d t_2 - \phi_0) = cos(2\pi + \omega_d t_1 - \phi_0) = cos(\omega_d t_1 - \phi_0) \tag{3.57}$$

from which follows

$$\delta = ln\frac{x_1}{x_2} = \zeta \omega_n \tau_d \tag{3.58}$$

and replacing the 3.56 in the 3.58 is found

$$\delta = \frac{2\pi}{\omega_d} \cdot \frac{c}{2m} \tag{3.59}$$

therefore being able to evaluate the damping coefficient by analyzing the system's response to a certain oscillation

49

in [19] there are several other methods to calculate the damping, with experiments done on a cantilever beam.

The use of the methods listed above leads to a more or less exact measurement of the damping to which the structure is subjected, but within this work it is not possible to calculate the damping by these methods as the response data in frequency of the real structure from which the damping can be obtained, for this reason inside the control part, to give a realistic effect of the structure response, it was decided to introduce a damping equal to 5% of the critical one for each d.o.f.

$$\zeta = 0.05 \rightarrow c = 2\sqrt{km} \cdot 0.05 \tag{3.60}$$

Chapter 4

Reconstruction

This chapter will explain the procedure for the reconstruction of the loads starting from the strains, which is the cornerstone of the thesis, then necessary for the analysis and the control. The need to reconstruct the external loads acting on the wing from the strains arises from the fact that having a time history of the strains, thanks to the FBGs installed on the structure, we are able to keep the deflections under control in some points of the structure. The points that need much more attention are those individuated from the preliminary analyses as the most critical. Once the entity and the distribution of the forces is known, through the control introduced by the ailerons and the mobile surfaces through their deflection, is possible to control the loads on the wing and then indirectly the deformation of the structure so that on one side it is able to guarantee a longer life to the structure, since the maximum loads suffered can be reduced, while on the other hand it opens up the possibility of a lighter structure as with the control of the loads is possible to reduce the stresses.

4.1   Sensitivity matrix

Since pressure-distribution method-based loads on a wing are usually not used except in specific cases where an accurate load distribution is desired, another method for load reconstruction is analysed in Skopinski (1953) [22], where is discussed the use of strain gages, their position in some points of

the structure and also their calibration.

We are able to write a system of linear equations that expresses the correlation between the strains and the applied forces as

$$\{\varepsilon\} = [C]\{F\} \tag{4.1}$$

where

- $\{\varepsilon\}$ is a $(n \times 1)$ vector of strains measured at n distinct locations

- $[C]$ is a $(n \times n_F)$ sensitivity matrix, with c_{ij} represents the strain at location i due to a unit load applied at location j

- $\{F\}$ is an $(n_F \times 1)$ vector of the n_F applied forces in the structure

The equation 4.1 create a correlation between the strains at any point in the structure and the forces acting on it, in the form of a linear combination of strains produced in a particular point by each of the applied loads. This causes the introduction of an approximation to a linear elastic problem assuming that the deformations are small enough that the superposition principle is valid. Assuming that $[C]$ is known and $\{\varepsilon\}$ is measured, the least-squares estimate of the unknown forces $\{F\}$ is given by

$$\{F\} = ([C]^T[C])^{-1}[C]^T\{\varepsilon\} \tag{4.2}$$

In the practical act of measurement, the strain vector is subject to errors, so that if the errors in the strain measure are independent and distributed identically, and the standard deviation of each of them is σ, then the variance-covariance matrix for the estimated loads is expressed as

$$var(\{F\}) = \sigma^2([C]^T[C])^{-1} \tag{4.3}$$

We have so that the matrix $([C]^T[C])^{-1}$ is called sensitivity of $[C]$. For a given variance in the strain measurement, the minimization of the $[C]$ sensitivity leads to an increase in the accuracy in the load estimation. The

sensitivity of $[C]$ is a function of the number, position and angular alignment of the strain gages installed on the structure. Therefore, an optimal selection of the positioning, the number and the angle can lead to a minimization of the sensitivity of $[C]$ and therefore lead to a better estimation of the loads. A procedure that can lead to minimization and therefore to a more precise load reconstruction can be divided in three phases with

1. generation of a candidate set;

2. determination of the number of strain gages that have to be used;

3. determination of the D-optimal design.

Candidate set

For the generation of the candidate set it must be taken into account that on the aeronautical structures there is a large number of locations where the strain gages can be installed. In particular, if we take into account that the FBG can be introduced inside the fiber layers of composite, the combination of possibilities increases a lot, always considering to not take in consideration all these positions that are not accessible or that could lead to excessive efforts in the structure, altering the result of the strain. Each position and angular orientation is determined with a candidate point, and each one of these points can determine a possible row within the matrix $[C]$. All possible combinations of positions and angular orientations constitute a set, then called a candidate set. The matrix $[C]$ is therefore only a subset of the candidate sets that gives me the most accurate reconstruction of the applied loads.

The candidate set can be generated analytically for a structure having any complexity through the use of the finite element model of the structure itself, even if there are some considerations to be made in the creation through this method. The finite element model must be prepared in such a way that all the surfaces from which the strain data can be extracted can be considered as a possible point of application of the strain gages, for example if we refer to the values of surface deformations the model can be created of shell type.

From a purely numerical point of view, it is preferred to use the central

value of the shell element instead of the one of a node, since the node of the surface can be a common node for four distinct surfaces, and therefore an average of the strain in that point of the four superficial elements. Once that is this value is obtained it must be taken into account that this value is measured with respect to the coordinated reference system of the element itself, positioned at the center of the element, so this means that also the angle between the reference system of the element and the global one has to be taken into account.
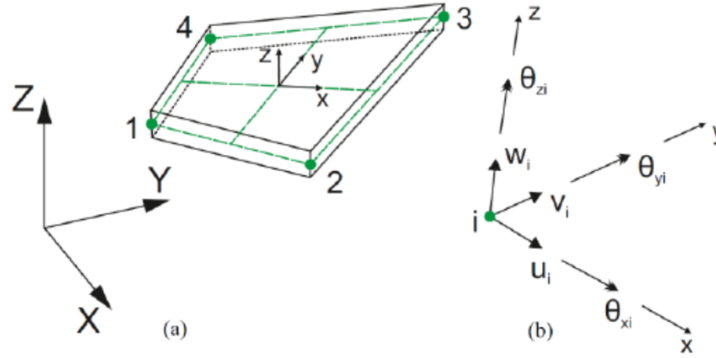

Figure 4.1.   Quadrilateral inverse shell element, showing global and local coordinate systems. (b) Nodal degrees of freedom in the local coordinate system xyz.

Unit loads are applied to the finite element model, one at a time, at the points corresponding to those where the unknown loads have to be reconstructed. For each applied unit load, the strain tensor is obtained for each of the elements corresponding to the positions in which a strain gage can be installed. Always taking into account the orientation of the various strain gages, we need to transform the strain tensor according to the global reference system, implementing a transformation from a reference system of the element xyz to a XYZ global one, as

$$[\varepsilon]_{XYZ} = [T][\varepsilon]_{xyz}[T]^T \qquad (4.4)$$

where $[T]$ denotes the transformation matrix that contains the direction cosines for the XYZ system with respect to the xyz system, and $[\varepsilon]_{XYZ}$ is the strain tensor, a (3×3) matrix containing the strains contributions.

Usually for the shell element, as the one used in this work FEM model, the z-axis has a normal direction respect to the plane of the element. Therefore, the strain transformations involve rotation about the z-axis with the

transformation matrix, is given by:

$$[T] = \begin{bmatrix} cos\theta & sin\theta & 0 \\ -sin\theta & cos\theta & 0 \\ 0 & 0 & 1 \end{bmatrix} \tag{4.5}$$

Number of strains

THe increasing of the number of the used strain gages increase the amount of information on the state of tension, helping to obtain a better reconstruction of the applied loads. From the practical and economic point of view there is a limit to the number of strain gages that can be used. It can be calculated that if the number of forces applied is n_F, then the number of strain gage used n must be $n \geq n_F$. If ε_{ei} denotes the experimentally measured strain from gage i and ε_{pi} denotes the predicted strain for gage i, using eq. 4.1, then the estimation error for gage i is given by

$$e_i = \varepsilon_{ei} - \varepsilon_{pi} \tag{4.6}$$

and for a system of linear equations with $n - n_F$ degrees of freedom, the variance in strain measurement errors is given by

$$\sigma^2 = \frac{\sum_{i=1}^{n} e_i^2}{n - n_f} \tag{4.7}$$

Given the maximum allowable variance in strain measurement errors that is acceptable, the number of required strain gages can be calculated using the equation 4.7.

4.2   Optimization

Given a strain gage number n, we look for a candidate set to find the gage locations and angular directions that give the least variance in the load reconstruction. There are several criteria that have been studied to decrease the sensitivity of the matrix $[C]$, and the criterion chosen, which also brings the best relevance with the case in question, is that which aims at maximizing $|[C]^T[C]|$, that is the determinant of $[C]^T[C]$. This type of optimization is called D-optimal design, where D stands for determinant. This criterion is used to select the best candidate points that can lead to the most accurate estimation of the loads.

4.2.1   D-Optimal

In order to be able to construct a D-optimal design for n points, the positions of the n strain gage and their angular orientations that maximize $|[C]^T[C]|$, must be selected by the candidate set. To do this, algorithms based on the principles of the optimal augmentation and reduction of an existing design can be implemented. Through an optimal augmentation, the candidate point with the greatest variance prediction is added in the form of a row to the matrix, so that the process of inserting and deleting candidate points goes on until the implementation of new rows does not lead to no improvement of the objective function.

The algorithm used to obtain the best candidate set is composed as follows: given the candidate set, a number n of usable strain gages and n_F applied forces, the first step is to take a candidate point n randomly from the candidate set so as to initialize the matrix $[C]_{n \times n_F}$. From the remaining candidate set, a candidate point is selected, and the corresponding row is added to matrix $[C]$, so that it becomes $[C]_+$, such that $|[C]_+^T[C]_+|$ is maximum. Next, out of the $n+1$ rows in matrix $[C]_+$, a row is deleted to arrive at matrix $[C]_-$ such that $|[C]_-^T[C]_-|$ is maximum. This process of augmenting and deleting rows continues until there is no further improvement in the value of $|[C]^T[C]|$. The final $[C]$ so obtained is the D-optimal design and provides the information on the optimum strain gage locations and angular orientations.
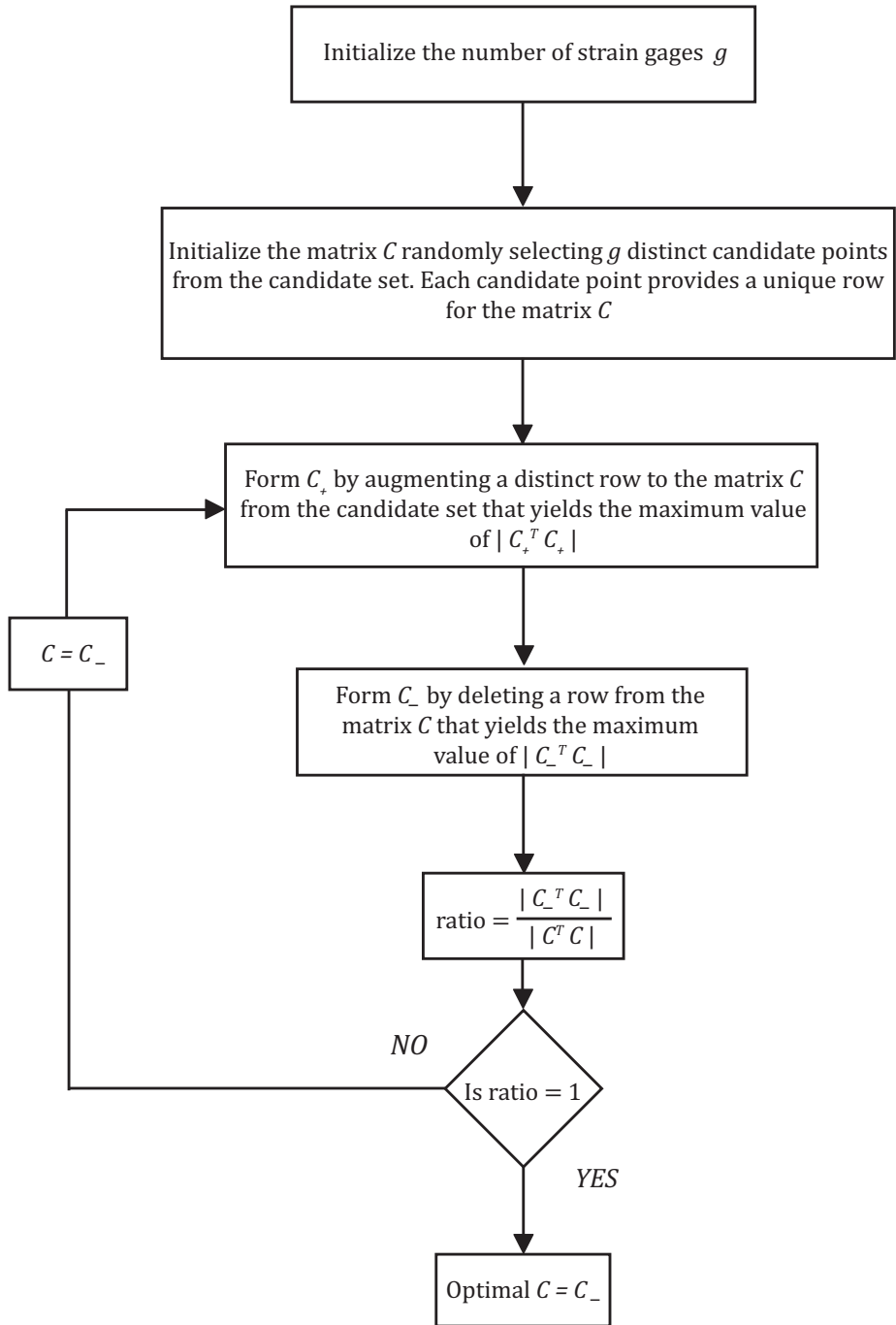
Figure 4.2.   Algorithm of the rows exchange

4.2.2 Concentrated Loads

For the reconstruction of the loads in the case of concentrated loads, 10 couples of loads have been applied, on the dependant node fn the MPC RBE3 of the corresponding rib, coinciding with the point of the rib that intercepts the elastic axis of the part to which the load is applied. Each load is composed by the force and a concentrated moment related to the various forces, introduced to include the transport moment for moving the forces from the quarter chord line to the elastic axis. Therefore, once the unit and total loads have been applied to the structure, in fig 4.3 and 4.4 the results of the reconstruction are shown, accompanied by the tables showing the values of the reconstruction, including those after optimization and the relative errors between the data applied and those reconstructed.
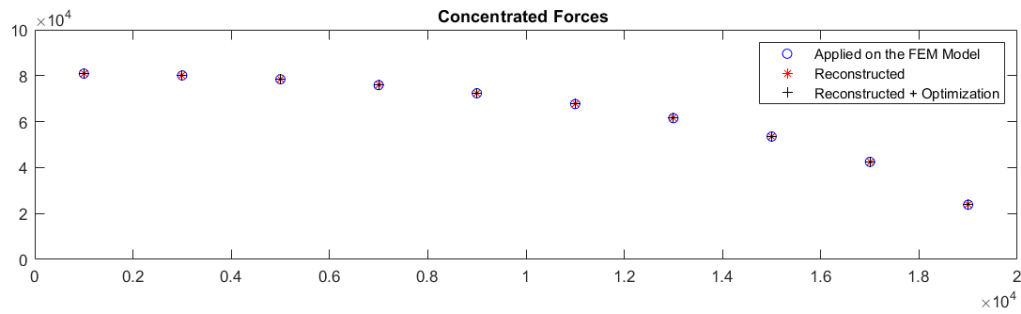

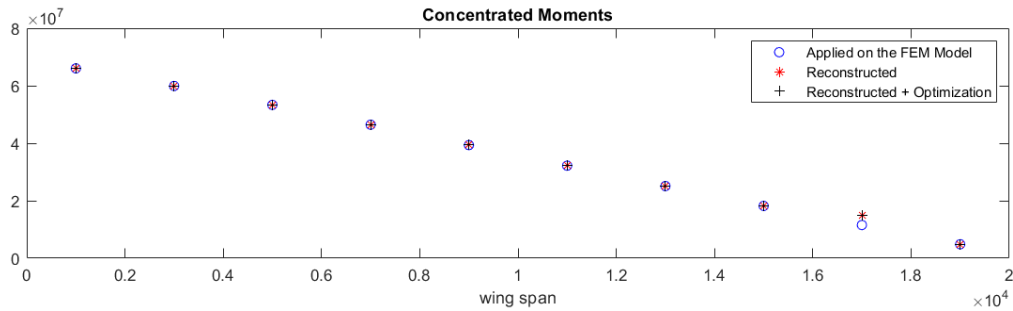Figure 4.3.   External concentrated forces reconstruction

Figure 4.4.   External concentrated moments reconstruction

In the figure 4.5 the elements identified by the D-optimal design for the reconstruction are highlighted. These element correspond to the position on which the strain gages should be installed for the best results. It is noted that these elements in the case of the concentrated loads are all positioned in

the front end of the structure, all identified either in the upper or the inferior spar, while in the rear part of the structure in the panels adjacent to the rear spar caps, and this is probably caused by the fact that such elements are the best one to reconstruct the loads since they are the furthest from the main elastic axis and therefore react more intensively to the stresses due to the torsion.
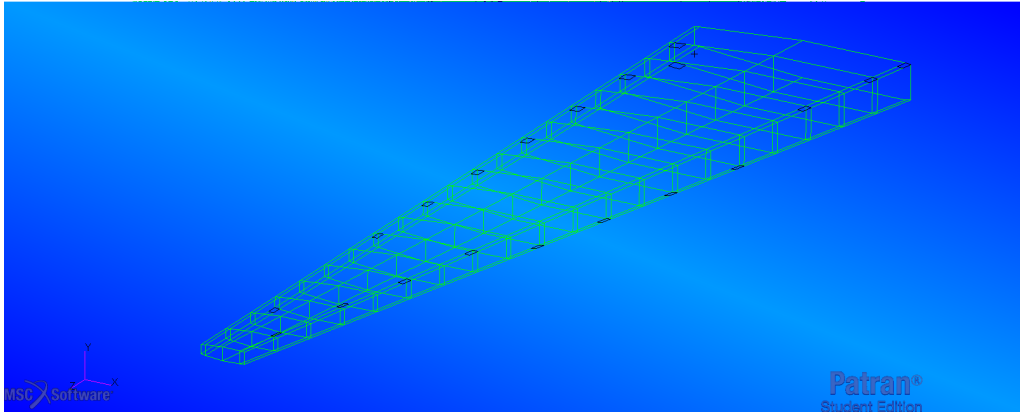

Figure 4.5.   Elements from D-Optimal Design

From fig. 4.3 and 4.4 is it possible to observe the results of the reconstruction. In the 4.3 is represented the reconstruction of the concentrated forces, and as reported in the table 4.2.2 is possible to see that the errors between the applied loads and the reconstructed ones are very small, considering an average error in the order of $1E - 4$, with the only exception of the F_8 force, which has a reconstruction with an error of an order of magnitude higher than the others, but which amounts to $1E - 3$, but still with an excellent level of confidence. An analogous consideration may be made concentrated moments, in 4.4, which however present a value of the moment M_9 with a reconstruction error, respect to the applied load of 29.38%. This value is not aligned with the other values of the reconstruction, which in fact, as shown in the table 4.2.2, excluding this element, have average errors of the order of $1E - 5$, with a minimum value of an order of magnitude lower. The fact that the moment M_9 does not respect the fidelity of reconstruction may be due not by a bad accuracy of the method, but a particular behaviour of the structure to that load, which therefore does not respond in a particularly linear way, just as it is necessary for reconstruction. It is also emphasized that for the purposes of this reconstruction only the strain values in the z direction were used, taking the local references of each element and rotating them to make them conform to the global reference axes, and

this could also contribute to in the measure of the moment concentrated out of scale.

Load	FEM Model load [N]	Reconstructed load [N]	Reconstructed load with optimization [N]
F_1	$8.0920E+4$	$8.0920E+4$	$8.0920E+4$
F_2	$8.0103E+4$	$8.0103E+4$	$8.0103E+4$
F_3	$7.8444E+4$	$7.8444E+4$	$7.8444E+4$
F_4	$7.5888E+4$	$7.5888E+4$	$7.5888E+4$
F_5	$7.2337E+4$	$7.2337E+4$	$7.2337E+4$
F_6	$6.7637E+4$	$6.7636E+4$	$6.7636E+4$
F_7	$6.1520E+4$	$6.1520E+4$	$6.1520E+4$
F_8	$5.3496E+4$	$5.3495E+4$	$5.3495E+4$
F_9	$4.2463E+4$	$4.2463E+4$	$4.2463E+4$
F_{10}	$2.3800E+4$	$2.3800E+4$	$2.3800E+4$

Table 4.1.   Values of the concentrated forces

Load	Error %	Error with optimization %
F_1	$-9.0414E-6$	$-7.9347E-5$
F_2	$+1.3801E-5$	$+5.0480E-5$
F_3	$-4.6097E-5$	$-2.6667E-5$
F_4	$-1.8330E-5$	$-2.9296E-5$
F_5	$-3.1206E-5$	$-2.5570E-5$
F_6	$-5.8048E-5$	$-6.1176E-5$
F_7	$+2.0935E-5$	$+2.1908E-5$
F_8	$-1.2174E-3$	$-1.2151E-3$
F_9	$+3.5449E-5$	$+3.8761E-5$
F_{10}	$+1.5827E-4$	$+3.8761E-5$

Table 4.2.   Values of the error in the concentrated forces reconstruction

From the data in the tables representing the errors in the reconstruction of the forces and concentrated moments before and after the optimization 4.2.2 and 4.2.2 it can be noticed that the data concerning the optimization are afflicted by a slightly higher percentage error than those of simple reconstruction. The reconstruction still have a good level of accuracy, since that the order of magnitude in the average error doesn't increase. The higher error is consequence of the fact that in the optimization are not used the data extracted from all the elements of the model but only by the ones obtained through the D-optimal design, such that the reconstruction is as

Load	FEM Model load [N]	Reconstructed load [N]	Reconstructed load with optimization [N]
M_1	$6.6031E+7$	$6.6031E+7$	$6.6031E+7$
M_2	$5.9917E+7$	$5.9917E+7$	$5.9917E+7$
M_3	$5.3342E+7$	$5.3342E+7$	$5.3342E+7$
M_4	$4.6443E+7$	$4.6443E+7$	$4.6443E+7$
M_5	$3.9352E+7$	$3.9351E+7$	$3.9352E+7$
M_6	$3.2195E+7$	$3.2195E+7$	$3.2195E+7$
M_7	$2.5100E+7$	$2.5100E+7$	$2.5100E+7$
M_8	$1.8189E+7$	$1.8189E+7$	$1.8189E+7$
M_9	$1.1550E+7$	$1.4942E+7$	$1.4942E+7$
M_{10}	$4.8553E+6$	$4.8553E+6$	$4.8553E+6$

Table 4.3.   Values of the concentrated moments

Load	Error %	Error with optimization %
M_1	$+2.8913E-6$	$+1.2008E-4$
M_2	$-7.9599E-6$	$-1.1420E-4$
M_3	$+1.0808E-4$	$+2.5322E-4$
M_4	$+8.9740E-5$	$+1.6211E-4$
M_5	$-1.2648E-5$	$+1.5961E-5$
M_6	$+1.8603E-5$	$+2.1660E-5$
M_7	$+3.6105E-5$	$+4.8832E-5$
M_8	$-1.1985E-4$	$-1.8377E-5$
M_9	$+2.9370E+1$	$+2.9370E+1$
M_{10}	$-7.1355E-5$	$-6.4127E-5$

Table 4.4.   Values of the error in the concentrated moments reconstruction

precise as possible using a much smaller data number. In particular for this model there are 4880 elements and in the optimization only 20 is used, that is the minimum since the rank of the $[C]$ matrix is also 20 or the number of concentrated forces and moments applied to the structure

	Value for Forces %	Value for Moments %
maximum error	$1.2175E-3$	$2.9370E+1$
maximum error with optimization	$1.2152E-3$	$2.9370E+1$
minimum error	$9.0414E-6$	$2.8913E-6$
minimum error with optimization	$2.1908E-5$	$1.5961E-5$
mean error	$1.6086E-4$	$2.9370E+0$
mean error with optimization	$1.7081E-4$	$2.9370E+0$

Table 4.5.   Errors in the concentrated loads

	max error %	min error %	mean error %
Value	$1.1985E-4$	$2.8913E-6$	$5.9876E-5$
Value with optimization	$2.5322E-4$	$1.5961E-5$	$9.0953E-5$

Table 4.6.   Concentrated moments loads, excluding M_9
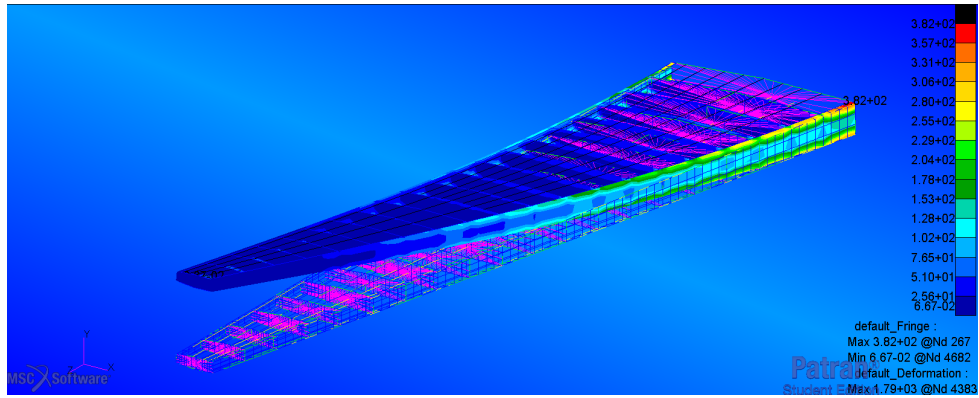
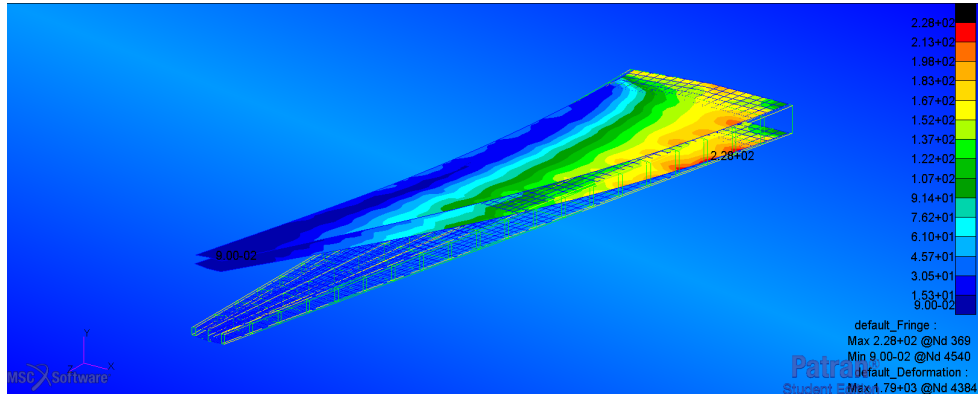Figure 4.6.   Stresses in spars and ribs due to concentrated loads

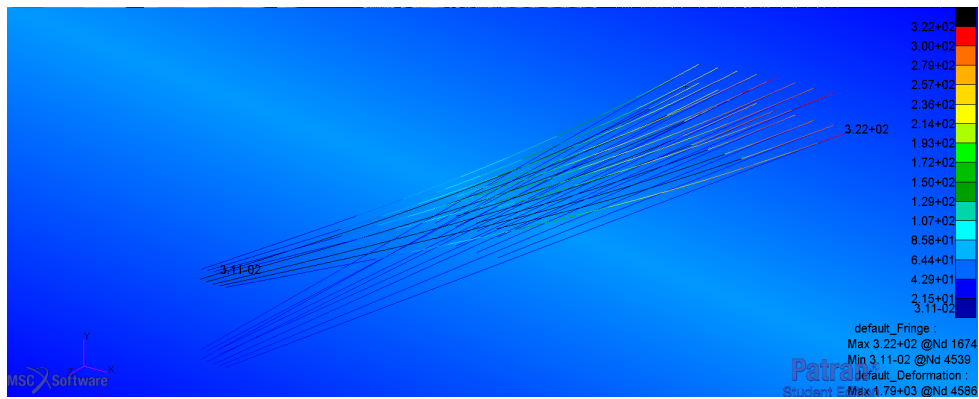Figure 4.7.   Stresses on skin panels due to concentrated loads

Figure 4.8.   Stresses in stringers due to concentrated loads

4.2.3 Distributed Loads

The reconstruction is now performed in the case of distributed forces: in our analysis we are dealing in particular with the distribution of both span-wise and chord-wise pressures, having in this way a 2D function distribution. Unlike the previous case here, although a $[C]$ matrix must be reconstructed anyway, the coefficients of this matrix are not the values of the strains after the unit forces will be applied, but coefficient linked to some basis functions. These basis functions are necessary because through their combination we are able to describe the function to be reconstructed. In this configuration we determine the coefficients c_{ij} of the sensitivity matrix as the coefficients of the linear combination of the functions. Having the function to be reconstructed, is it possible to write

$$F(x) = c_1 \cdot f(x)_1 + c_2 \cdot f(x)_2 + \ldots + c_n \cdot f(x)_n \qquad (4.8)$$

where the coefficients c_i represent the weights of the various basis functions for the reconstruction of the function $F(x)$. It is very important, in the selection of the basis functions, to choose functions that are linearly independent from each other, so as to have a solid function base and which allows a $[C]$ reconstruction matrix of maximum rank. For the reconstruction of the lift function, the basis functions that have been chosen are

$$\{f(z)\} = \begin{cases} f(z)_1 = 1 - \xi \\ f(z)_2 = 1 - \xi^2 \\ f(z)_3 = 1 - \xi^3 \\ f(z)_4 = 1 - \xi^4 \\ f(z)_5 = \sqrt{1 - \xi} \end{cases} \qquad (4.9)$$

where $\xi = \dfrac{z}{l}$ and l is the value of the wing span. As we note the function vector $\{f_z\}$ is expressed only in terms of the z coordinate, because the distribution of the function along the chord has been chosen as a ramp function, which takes on value unitary to the tailing edge, and instead zero value to the tailing edge, then like

$$f(x) = \frac{x}{c} \tag{4.10}$$

where c is the chord of the wing, which varies as

$$c(z) = c_r - \frac{c_r - c_t}{l \cdot z} \tag{4.11}$$

thus having the vector of functions in two dimensions as

$$\{f(z,x)\} = \{f(z)\} \cdot \frac{x}{c_r - \frac{c_r - c_t}{l \cdot z}} \tag{4.12}$$
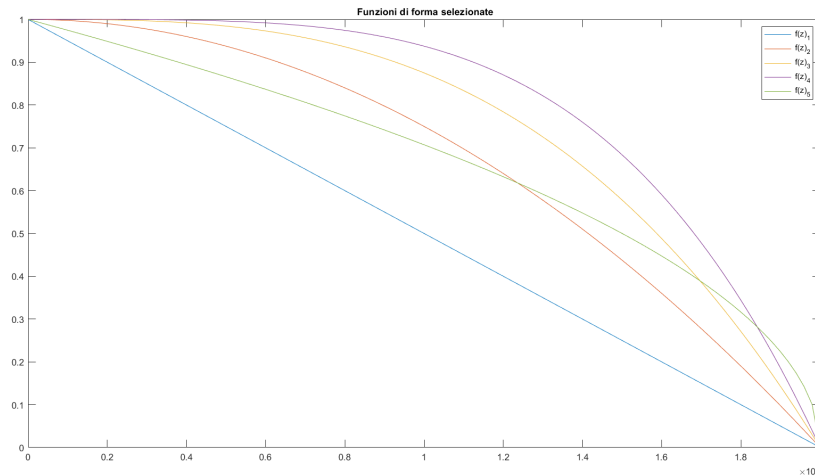

Figure 4.9.   Basis functions selected for reconstruction

The fact of having opted for an elliptical distribution instead of a distribution that respected the shape of the wing plan, thus going to define a descending ramp-like shape added to a step, was made to better show the reconstruction and reliability of the method. A lift function as the one of the chord in eq 4.11 would have required only two functions of shape, step and ramp. The elliptical one allows us to use a complete and linear base of functions independent, excluding however a basic elliptical function.

Once the functions that compose the base have been selected, they are applied, as in the case of concentrated loads, to the structure with unitary

values, so as to record the structure response to these efforts and thus to construct the matrix $[C]$ using the data of the various basis functions.
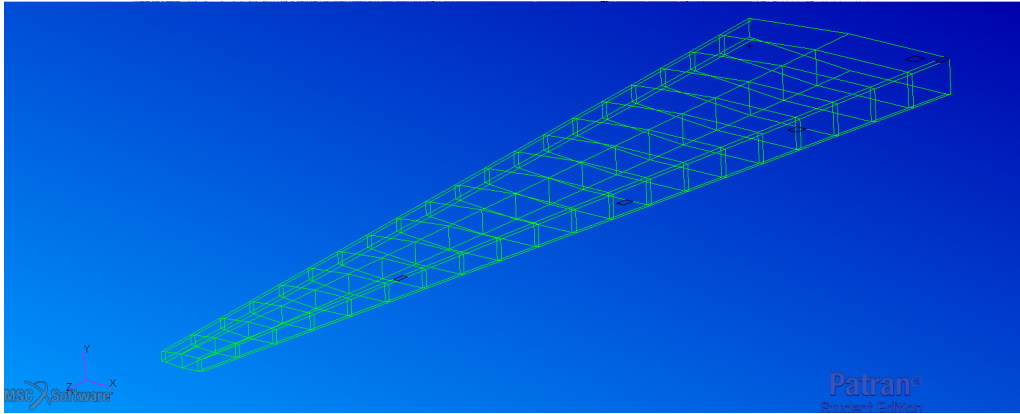

Figure 4.10.   D-Optimal design elements position

In figure 4.10 the elements identified by the D-optimal design for reconstruction in the case of distributed loads are highlighted. Here, unlike in the case of concentrated loads, the selected elements are all in the front of the structure and 3 of them in a position corresponding to approx $\frac{1}{3}$ of the chord, probably du to the fact that in that area the influence of the pressure distribution increases.

It is then finally shown in the figure 4.11 the reconstruction of the distribution of forces applied to the model, plotting the value of this distribution at the leading edge point, since the distribution along the chord goes from this value to zero on the rear spar. From the data is it possible to observe excellent results, with low percentage errors. In particular in the table 4.2.3 the values of the weight coefficients for the various functions of the base are shown, comparing the values obtained from the linear combination applied to the distribution of forces, and their reconstructions before and after the optimization. An analysis of the most significant values is made, so to evaluate the error in the reconstruction, both as regards the coefficients and for the final function, reported in table 4.2.3. From this table it is clear that despite the coefficient reconstruction values are affected by an average error of the order of $1E+0$ the consequent combination of functions to compose the complete function leads to an error in the values of the function much smaller, with average values of the order of $1E-3$. This means that, compared to the case of concentrated forces, there is a bigger error, but that it is linked to the more complex response of the structure, which in this case is subjected not to concentrated, but distributed forces.
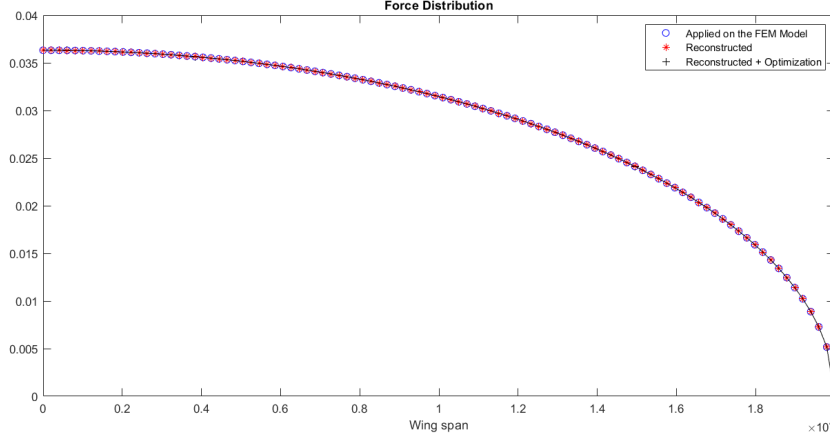
Figure 4.11.   Distributed load reconstruction

$\{f(z,x)\}$	c_i FEM applied	c_i reconstructed	c_i reconstructed + optimization
f_1	$-2.6051E-2$	$-2.6128E-2$	$-2.5982E-2$
f_2	$+1.2481E-2$	$+1.2710E-2$	$+1.2002E-2$
f_3	$-4.6582E-3$	$-4.9132E-2$	$-3.8649E-3$
f_4	$+2.7220E-3$	$+2.8216E-3$	$+2.2897E-3$
f_5	$+5.1872E-2$	$+5.1822E-2$	$+5.1880E-2$

Table 4.7.   Coefficients c_i

	Value coefficients c_i %	Value distribution $L(z,x)$ %
maximum error	$5.4740E+0$	$2.3436E-2$
maximum error with optimization	$1.7031E+1$	$5.7860E-2$
minimum error	$9.9691E-3$	$5.4267E-6$
minimum error with optimization	$1.0223E-1$	$1.7601E-4$
mean error	$2.2546E+0$	$4.1161E-3$
mean error with optimization	$7.4232E+0$	$6.8374E-3$

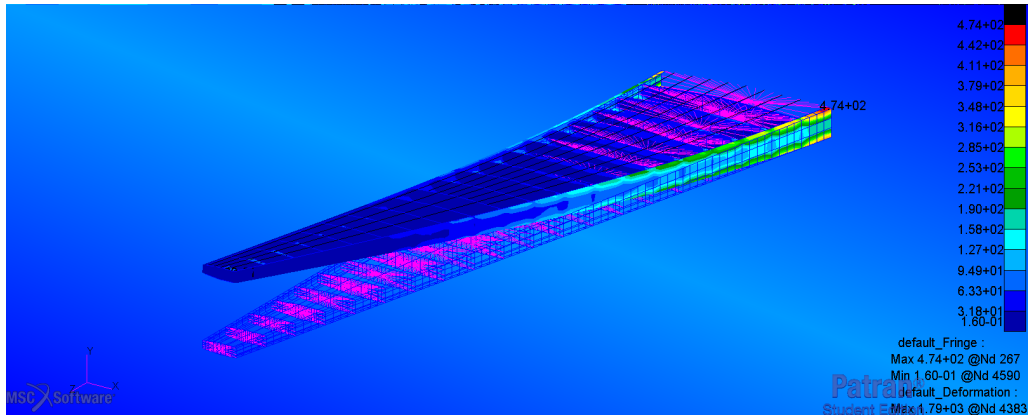Table 4.8.   Comparison of errors in the reconstruction of distributed loads
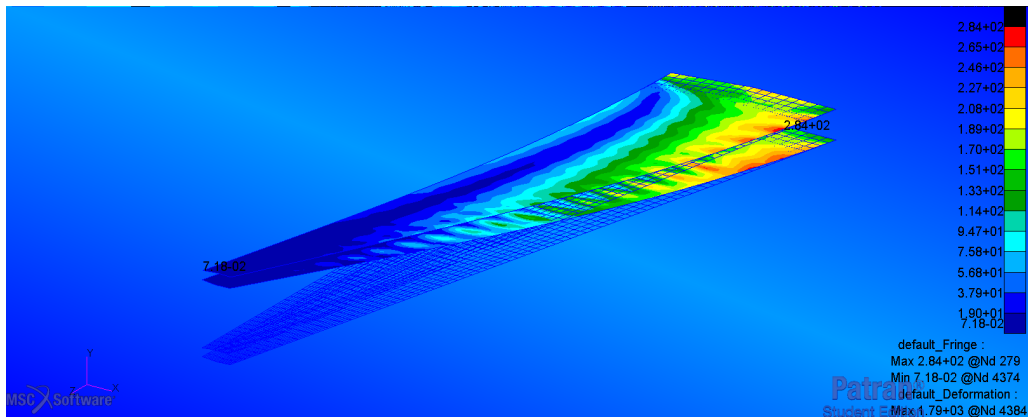
Figure 4.12.   Stresses in spars and ribs
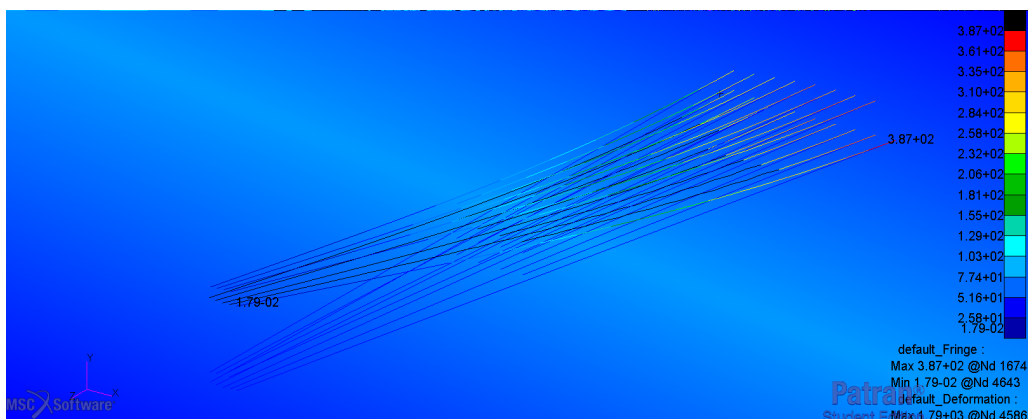

Figure 4.13.   Stresses on skin panels

Figure 4.14.   Stresses in stringers

Chapter 5

Control System Design

The knowledge of the stresses, moments and forces acting on the aircraft is useful to control the dynamic behaviour of the analysed system. The control system should be able to reduce the forces acting on the wing and the damage due to the deformations, that are generated by a disturbance. Thanks to the control surfaces, the objective of the control system is to reduce the deformations and stresses acting on the aircraft after a gust. Through the use of the ailerons, used for the rolling attitude control, being able to variate the angle of these ailerons it is possible to generate a lift variation which aims to reduce the aerodynamic loads acting on the structure, in order to reduce the internal stresses. In the following analysis a disturbance due to a gust during a flight will be taken into consideration, and a control will be performed through the variation of the angle of the mobile surfaces to reduce the deflections to which the wing would be subjected.

5.1   Gust

Taking into account the regulations given by the European Aviation Safety Agency (EASA) (paragraph CS 25.341 in [7]) the shape of the gust is given as a form called $1 - cos$ which is identified as

$$v_g = \begin{cases} \frac{U_{gust}}{2}[1 - cos\left(\frac{\pi s}{H_g}\right)] & 0 < s \leq 2H \\ 0 & s > 2H \end{cases} \quad (5.1)$$

where s is the penetration distance of the gust, measured in meters. H instead is the gradient of gust, also measured in meters, while U_{gust} is gust speed at equivalent air speed, given by the following formula

$$U_{gust} = U_{ref}F_g \left(\frac{H_g}{107}\right)^{1/6} \quad (5.2)$$

with U_{ref} which in this case is $17.07\,\mathrm{m/s}$, F_g having the value of the first bending frequency of the structure, making sure that the gust frequency matches that of the first natural frequency of the structure, in this case the bending one, maximizing its impact on the wing. A summary of the data concerning the gust and its shape can be found later

V	Flight speed	$164.6\,\mathrm{m/s}$
h	Altitude	$6096\,\mathrm{m}$
H_g	Gust gradient	$26\,\mathrm{m}$
U_{ref}	Gust value	$17.07\,\mathrm{m/s}$
F_g	First bending frequency	$2.39\,\mathrm{Hz}$

Table 5.1.   Gust values

The aircraft control surfaces are aerodynamic devices that allows the pilot to control the aircraft's flight and to adjust its attitude. In particular the aileron is an hinged flight control surface that is usually placed in the trailing edge of each wing of a fixed-wing aircraft, and is used to control the aircraft in roll.

Defining as δ_A the angle that is created between the zero lift line of the aileron and that of the entire profile when the aileron is in the rest position. Through the variation of this angle it is possible to vary the aerodynamic forces acting on the profile as it is

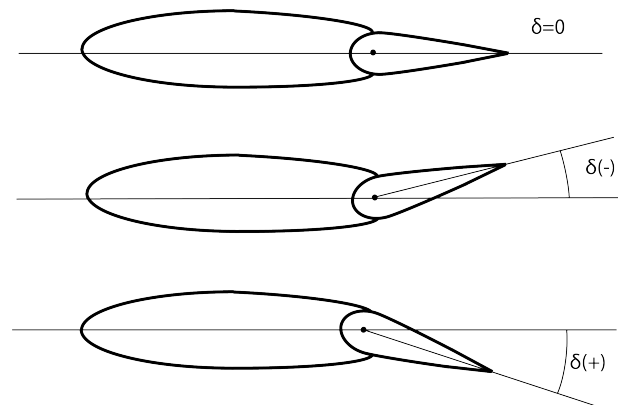$$L = \frac{1}{2}\rho S V^2 \left(C_{l_\alpha} \cdot \alpha + C_{l_{\delta_A}} \cdot \delta_A\right) \quad (5.3)$$

Figure 5.1.   Aileron

where α is the angle of inclination between the speed of the flow that invests the profile and the zero lift line of the profile, C_{l_α} represents the variation of the lift coefficient as a function of the inclination angle, and $C_{l_{\delta_A}}$ similarly it represents the variation of the coefficient of lift due to the variation of δ_A, depending only to the ailerons.

Given the eq. 5.3, given an negative angle δ_A there is a decrease of the lift forces, used in a gust load scenario, to reduce the loads on the structure. Within this work it was therefore decided to divide the lift acting on the wing into two contribution: the one due to the inclination angle α, and a negative force generated by the aileron deflection, in order to simplify the problem by decoupling the two contributions. In this way two different sets of forces acting on the system are created. This decomposition is a simplification of the real condition, since in this case the two forces have simply been superimposed. It's not taken into account the aerodynamic of the wing, and the variation in the forces distribution if the mobile surfaces are actuated. In fact their movement, modifying the pressure distribution around the profile, could lead to a generation of twisting forces on the wing, due to the distance from the elastic axis.

In chapter 3 the distribution of the lift on the wing was discussed, proposing both the model with concentrated loads and the one with distributed loads. What was said for the entire structure can also be done as regards the aileron. But, in the control analysis, was decided not to consider the distributed model, focusing only on the effect of the concentrated loads, since it is the one applied to the beam-like structure to be controlled. The shape of the load, acting on the structure in the areas of the aileron, has

been decided to be a ramp shape, taking into account into account the chord of the section, given that the aileron is assumed constant.
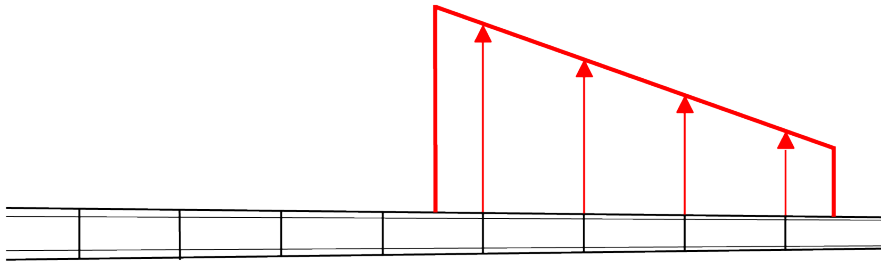
Figure 5.2.   Aileron lift force due to δ_A

Similarly to what has been done for the case of the concentrated forces, once the shape has been defined, it has been decomposed into concentrated contributions, applying them to the control model, thus becoming the control component of the system which is predisposed to control the wing deflection.

It is also noted that being from eq. 5.3 the speed composition of the flight speed and of the gust speed can be written

$$L = \frac{1}{2}\rho S(V + v_g)^2 \left(C_{l_\alpha} \cdot \alpha + C_{l_{\delta_A}} \cdot \delta_A \right) \tag{5.4}$$

having therefore that the component due to the aileron is

$$L_\delta = \frac{1}{2}\rho S(V + v_g)^2 C_{l_{\delta_A}} \cdot \delta_A \tag{5.5}$$

therefore having to also take into account the contribution of the increase in speed within the variation of the aileron, as an additional contribution

to the control.

5.2   Design of Linear Quadratic Regulator

The Linear Quadratic Regulator is an optimal control technique that provides the best possible performance with respect to certain performance measures. The design problem with LQR is to turn off a state feedback controller K such that the objective function J is minimized. In this method, a feedback gain matrix is designed, that minimizes the objective function so as to reach a compromise between the force in the use of control, the magnitude, and the responsiveness to guarantee a stable system. For a continuous linear system in time described as

$$\dot{x} = Ax + Bu \tag{5.6}$$

with a cost function defined as

$$J = \int_0^\infty (x^T Q x + u^T R u) dt \tag{5.7}$$

where Q and R are the weight matrices; Q must necessarily be a positive or semipositive symmetrically defined matrix; R must be a positive definite symmetric matrix. A practical method for choosing Q and R is that they are diagonal matrices. The value of the elements in Q and R is related to their contribution in the cost function. By making sure that the control law minimizes the value of the cost function, there is feedback like

$$u = -Kx \tag{5.8}$$

with K obtained as

$$K = R^{-1} B^T P \tag{5.9}$$

and where P is obtained from the resolution of the continuous time Algebraic Riccati Equation (ARE)

$$A^T P + PA + Q - PBR^{-1}B^T P = 0 \qquad (5.10)$$

The control design to find a feedback gain for the LQR can then be summarized in the following steps:

- Selection of the design parameters in the form of the matrices Q and R

- Find a P to solve ARE

- Find the state feedback matrix K using $K = R^{-1}B^T P$.

In order to achieve zero steady state error, an integral action is included within the LQR controller. The basic approach that is used in the integral feedback is to create a state with a controller that computes the integral of the signal error, which is then used as a feedback term. This is done by increasing the system description through a new z state:

$$\frac{d}{dt}\begin{bmatrix} x \\ z \end{bmatrix} = \begin{bmatrix} Ax + Bu \\ y - r \end{bmatrix} = \begin{bmatrix} Ax + Bu \\ Cx - r \end{bmatrix} \qquad (5.11)$$

where the final compensation is given by

$$u = -K(x - x_e) - K_i z + u_d \qquad (5.12)$$

5.2.1 Mathematical model of the System

Before proceeding with the results of the control with the system forced by gust loads, given that the LQR system provides a linear system of type $dotx = Ax + Bu$, the current second degree system must be brought back to a similar system. From the definition of our system as

$$[M]\{\ddot{x}\} + [C]\{\dot{x}\} + [K]\{x\} = \{F\} \tag{5.13}$$

we can define inside the forces and moments vector $\{F\}$ all the external contributions that interact with our system as forces and moments, so we can write

$$\{F\} = \{F_B\} + \{F_g\} \tag{5.14}$$

where $\{F_B\}$ includes all the forces and moments generated by the deflection of the mobile surface δ_A, while $\{F_g\}$ represents the external disturbances introduced by the gust in our case under examination. The forces F_B are expressed as

$$\{F_B\} = \{F_{\delta_A}\} \cdot \delta_A \tag{5.15}$$

where δ_A is the aileron deflection, and F_{delta_A}, referring to eq. 5.5, is

$$F_{\delta_A} = \frac{1}{2}\rho S(V + v_g)^2 C_{l_{\delta_A}} \tag{5.16}$$

Performing a change of variables as follows

$$z = \left\{ \begin{array}{c} z_1 \\ z_2 \end{array} \right\} = \left\{ \begin{array}{c} x \\ \dot{x} \end{array} \right\} \tag{5.17}$$

is it possible to write, taking into account eq. 5.13

$$\dot{z} = \left\{ \begin{matrix} \dot{z}_1 \\ \dot{z}_2 \end{matrix} \right\} \rightarrow \dot{z} = \left\{ \begin{matrix} z_2 \\ -[M]^{-1}[K] - [M]^{-1}[C] + [M]^{-1}\{F\} \end{matrix} \right\} \qquad (5.18)$$

thus being able to write our system as

$$\dot{z} = Az + Bu + Ed \qquad (5.19)$$

where

$$\dot{z} = \left\{ \begin{matrix} \dot{x} \\ \ddot{x} \end{matrix} \right\} \quad \text{and} \quad z = \left\{ \begin{matrix} x \\ \dot{x} \end{matrix} \right\} \qquad (5.20)$$

$$A = \begin{bmatrix} 0 & 1 \\ -[M]^{-1}[K] & -[M]^{-1}[C] \end{bmatrix} \qquad (5.21)$$

$$B = \begin{bmatrix} 0 \\ [M]^{-1}\{F_\delta\} \end{bmatrix} \qquad (5.22)$$

$$u = \delta \qquad (5.23)$$

$$E = \begin{bmatrix} 0 \\ [M]^{-1}\{F_g\} \end{bmatrix} \qquad (5.24)$$

Note therefore that the A matrix corresponds to the state matrix, the B matrix is the matrix that multiplies the input δ_A our aileron variation, and Ed that corresponds to the external inputs, in the form of accelerations, which introduces the gust into my system, with E which contains within it all the normalized aerodynamic coefficients with respect to the mass, and d which indicates which degrees of freedom are affected by the disturbance.

As denoted in [24] the reduction of the system from n equations of the second order to $2n$ equations of the first order produces a system matrix
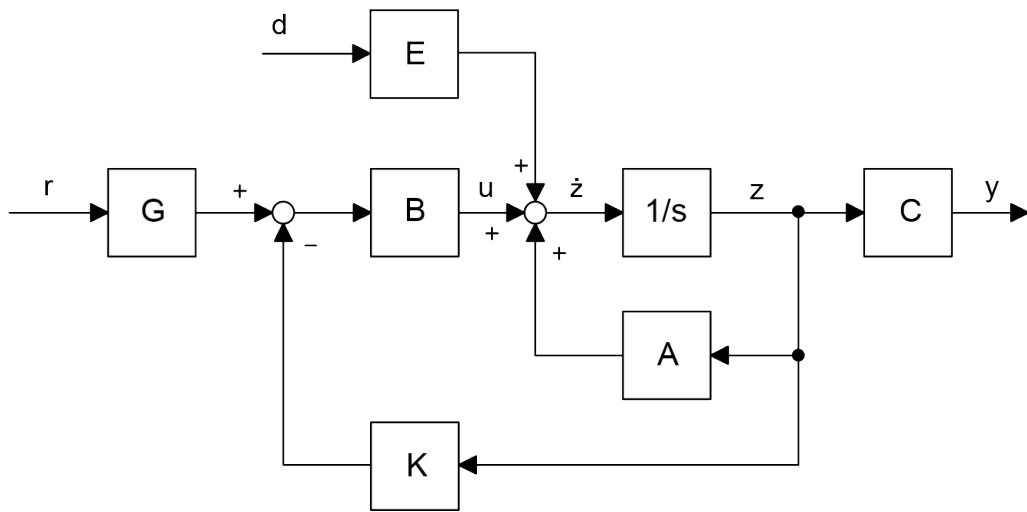
Figure 5.3.   System block diagram

which is not symmetrical, and eventually this can lead to a non symmetric eigenvalue problem which is a drawback of this formulation. The solution for this eigenvalue problem can be obtained through various iterative methods. In particular, the eigenvalue problem is obtained by inserting the solution of the equation within the original equation; in the case of free vibration, we have

$$\dot{X} = AX \qquad (5.25)$$

For the first order matrix differential equation we can assume a solution of this type

$$X = \sum C_i e^{\lambda_i t} \qquad (5.26)$$

where here C_i represent the vector which contains the constants that are obtained by the initial conditions, and λ_i has to be obtained using the solution inside the space-state equation in the homogeneous care, as

$$\lambda_i X = AX \qquad (5.27)$$

77

from which it follows

$$(A - \lambda I)X = 0 \tag{5.28}$$

which corresponds to the problem with standard eigenvalues, with the difference in this case that A is a non-symmetric matrix. The solution to the eigenvalue problem posed as a state space equation must give $2n$ complex eigenvalues and complex of matrix A. This $2n$ set consists of n eigenvalues and n conjugates, which means that the eigenvalues and their eigenvector correspondences are in conjugate pairs. Diagonalizing the matrix A, the equations are decoupled and solved for the individual variables. First of all, we must obtain the vectors that diagonalize the matrix. Having that

$$AV_j = \lambda_j V_j \tag{5.29}$$

$$W_j^T A = \lambda_j^* W_j \tag{5.30}$$

with every V_j such that

$$(A - \lambda_j I)V_j = 0 \tag{5.31}$$

and every W_j that suits

$$W_j^T (\lambda_j^* I - A) = 0 \tag{5.32}$$

Pre multiplying the two eigenproblems for V_j^T and V_j^T respectively, one can find that the eigenvectors of A and the left eigenvectors of A have the same values:

$$W_j^T A V_j = \lambda_j W_j^T V_j \tag{5.33}$$

$$V_j^T A^T W_j = \lambda_j^* V_j^T W_j \tag{5.34}$$

$$(V_j^T A^T W_j)^T = W_j^T A V_j \qquad (5.35)$$

$$W_j^T A V_j = \lambda_j^* W_j^T V_j \qquad (5.36)$$

follows that

$$\lambda_j^* = \lambda_j \qquad (5.37)$$

In this way it is shown that the left eigenvectors of A are also eigenvalues of A^T

in [24] it is also shown, besides the fact that the eigenvalues of A and A^T are the same, that to decouple the two equations are necessary $2n$ orthogonal eigenvectors, then is tested the orthogonality between the eigenvectors of A and A^T so that they are orthogonal to each other.

5.2.2   Stability and controllability

Once we have defined our system, which corresponds to a second-order system, before to proceed with the control it is good to check its values from the point of view of stability, and if it is controllable. First of all we must evaluate the stability of the system, that is, if given an external perturbation to the system of limited duration, its response is limited and converges to a condition of equilibrium. To evaluate the stability of our system we study the roots of the associated characteristic equation in the form

$$a_0 \lambda^2 + a_1 \lambda + a_2 = 0 \qquad (5.38)$$

where $a_0, a_1 e a_2$ are constant values and λ are the eigenvalues of the equation, thus having a stable system if, in the case of roots in complex form, their real part is negative, so if

$$\lambda = \lambda_r + \lambda_i \rightarrow Stability \Leftrightarrow \lambda_r < 0 \tag{5.39}$$

Therefore, deriving the roots of the characteristic equation of our system, which correspond to the eigenvalues of the same, it is possible to notice that our system is stable, as shown in the figure 5.4, where the poles of the system are represented in the complex plan
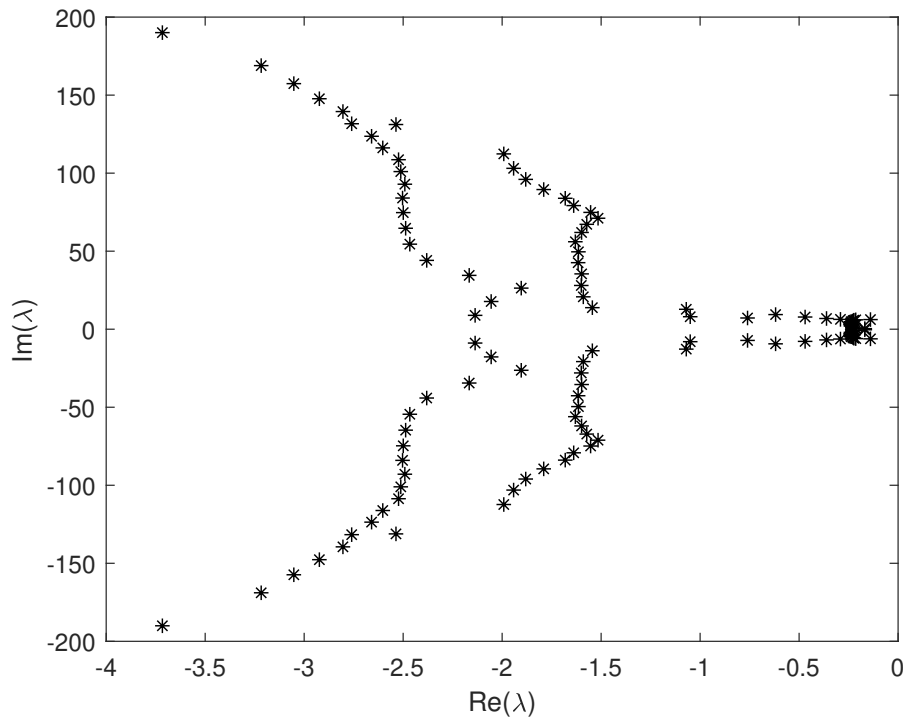

Figure 5.4.   Eigenvalues of the system

Focusing now on the controllability of the system, defining a controllable system if it is possible to reach any of its configurations in a finite time, through an input function, or forcing, to the system. In particular for a dynamic linear system like ours

$$\dot{x}(t) = Ax(t) + Bu(t)$$
$$y(t) = Cx(t) + Du(t) \tag{5.40}$$

it is controllable if its controllability matrix

80

$$R = [B\ AB\ A^2B\ \dots\ A^{n-1}B] \qquad (5.41)$$

has all columns or rows linearly independent, i.e. with rank n, where n number of system states. In our case $n = 4$, since the system states are dependent on each other. The forcing, within the array $[B]$, act only on the translation on y axis, then directly on the deflection v and the bending θ_x, and on the rotation around z, so on the twist θ_z. Since for the construction of the stiffness matrix, v and θ_x are dependent on each other, and that θ_z is independent to all other d.o.f., this means that the maximum rank of the controllability matrix is 4, which means that our system can also be controlled.

5.3   Simulation Results

Finally, the results related to the control of the system are shown below through the use of the forcing introduced by the ailerons. The vertical deflection values of the v structure along the y axis, the corresponding flexural rotation θ_x around the x axis and the twist rotation θ_z have been taken into consideration around the axis z, representing in the various graphs the value of the known final structure. Given the structure of the system, which includes an external forcing, two types of control for the system were tested: in fact, since the forcing is external to the system, it has been possible to set the reference that the controller K must follow in two ways, that in one case it has been set to 0 making the system controlled in order to dampen the effects of the external forcing going to stabilize to an equilibrium condition imposed by the forcing, making sure that when the system suffers the gust, the controller does nothing but dampen this effect by following its course; another type of control was to make the controller intervene to minimize the difference between the system's response and a threshold value, making sure that once the forcing due to the gust is received, the system is forced by the controller K to return to a value lower than the equilibrium condition.

In the figure 5.5 the trends of the variation of the δ_A aileron angle over time are reported, in the two control cases, from which it can be seen that, in the case of reference equal to 0, the angle has an angle variation with a higher slope and which reaches a higher value, equal to approx $-1.8°$ and then tend to return to an equilibrium position, assuming a smaller positive
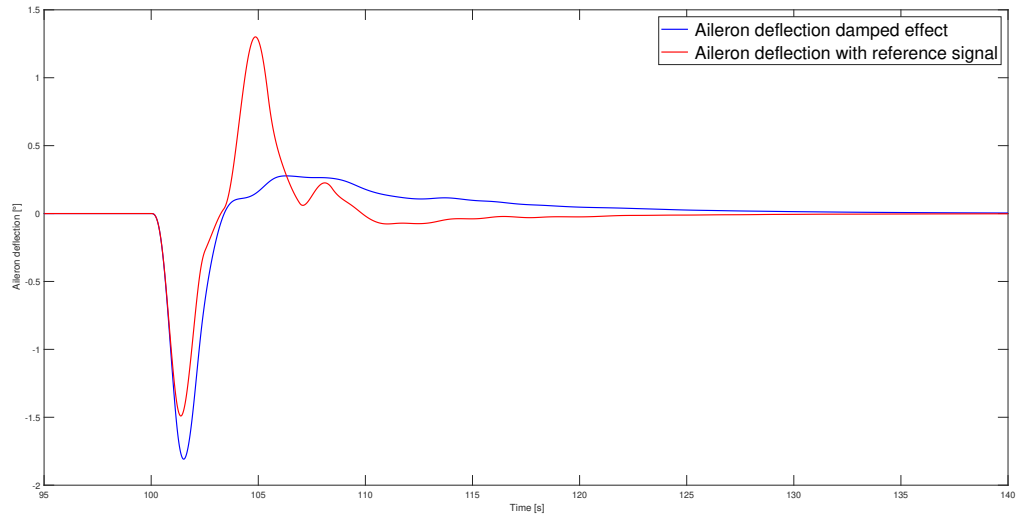
Figure 5.5. Deflection of δ_A angle during the control

value due to the avoidance of overshooting; while in the case of the reference one has a value of δ_A which reaches a lower value than the previous one, but then goes on to assume a positive value of approximately equivalent intensity, due to the greater oscillations that the system undergoes in this case.
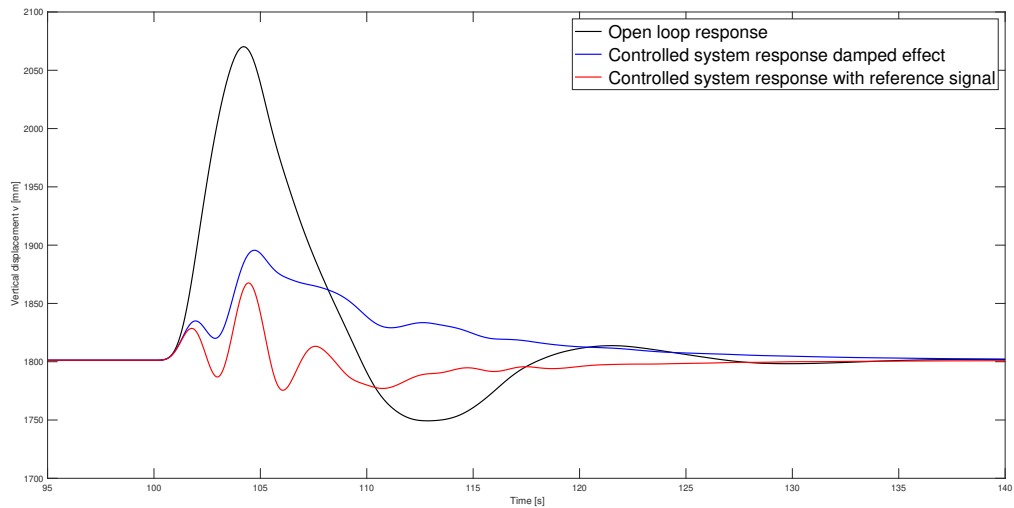
Figure 5.6. Comparison between the deflection response v

It can be seen from the comparisons that regarding the v deflection and the θ_x flexural rotation, which are related to each other by the stiffness

82
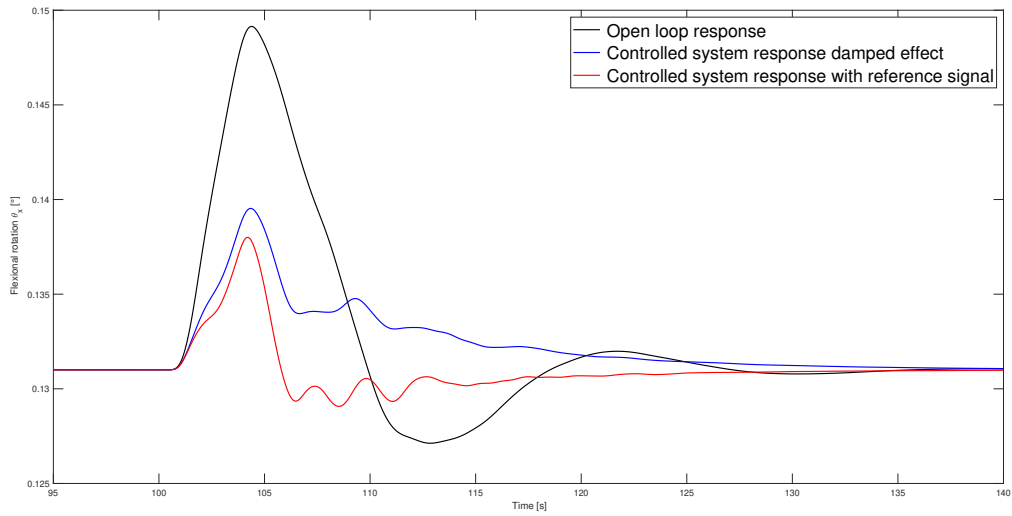
Figure 5.7.   Comparison between the flexural response θ_x
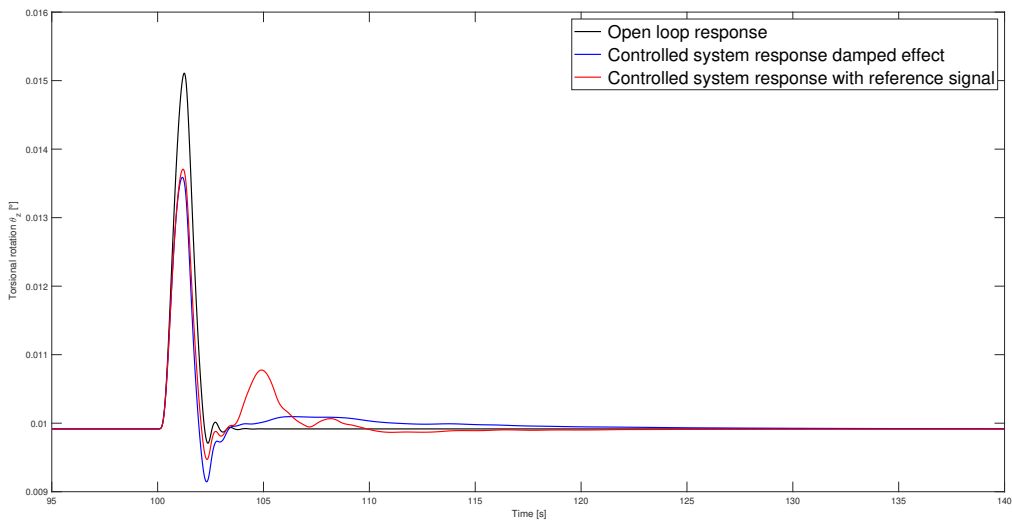
Figure 5.8.   Comparison between the torsional response θ_z

matrix, we have, in the case of null reference, a response that takes on a greater but more gradual and attenuated value over time while for that with a reference signal there is a lower maximum value but with some oscillations around the equilibrium condition due to the type of control, which activates only if the deflection exceeds a certain threshold and is no longer active when value falls below the threshold value. A slightly different consideration must be made regarding the torsion, since for it the control has been indirect, since

83

the references and the threshold values have been set for the deflection, and therefore the torsion response is a consequence of the implementation of the ailerons for deflection control. Another point of analysis is that of the speed of the response, that the deflection and deflection is much slower than that of torsion, due to the dynamic properties of the various displacements, which in this case are different from each other.

	Open Loop response	Controlled system response damped effect	Controlled system response with reference signal
v [mm]	2070.2	1895.59	1867.59
θ_x [°]	0.1491	0.1395	0.1380
θ_z [°]	0.0151	0.0136	0.0137

Table 5.2.   Maximum values during the gust

Given that through the control of the deflections and of the rotations of the structure is accomplished the internal stresses control, here below are reported the results concerning this control, and in particular we refer in particular to the internal efforts concerning the condition of maximum deflection of the wing, as it is the one to which the greatest forces correspond. To the condition of maximum deflection in the case of a free system, a system with aileron control with and without a reference signal, refer to the figures from 5.9 to 5.17 in which the internal stresses of the stringers are highlighted, referring to the axial stresses, as they are the ones that most characterize them, of the skin panels, analyzed in their outer layer, and finally of the side members, ribs and spar caps in the three conditions.

As regards the distribution of the stresses concerning spar caps and spars in particular, a greater concentration of stresses is noted in the area of intersection between the spars and panels, in correspondence with the spar caps, which is the maximum concentration point in the section, in particular to the root of the structure, and this is due to the fact that in that area, being the structure constrained, there are the greatest concentrations of stresses.

Similarly to what has been observed for the spar and spar caps, in the panels too, have a stress distribution that goes from the root to the extremity, with a greater concentration in the front part of the structure, due to the greater rigidity in that part, which therefore leads to greater stresses.
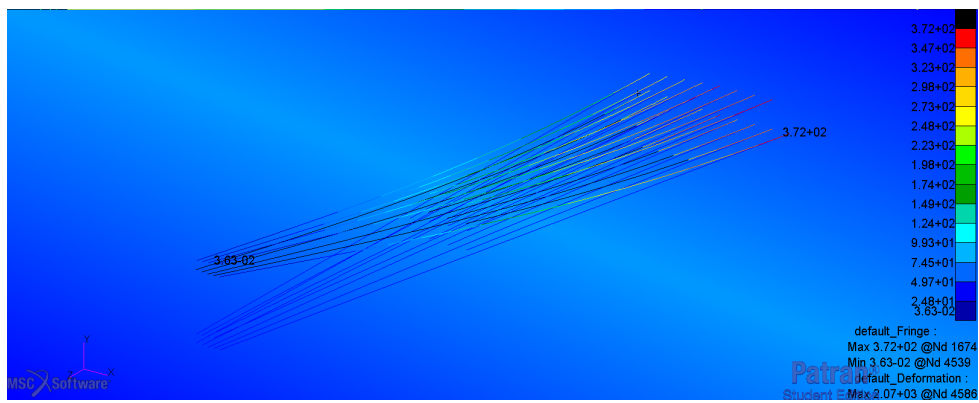
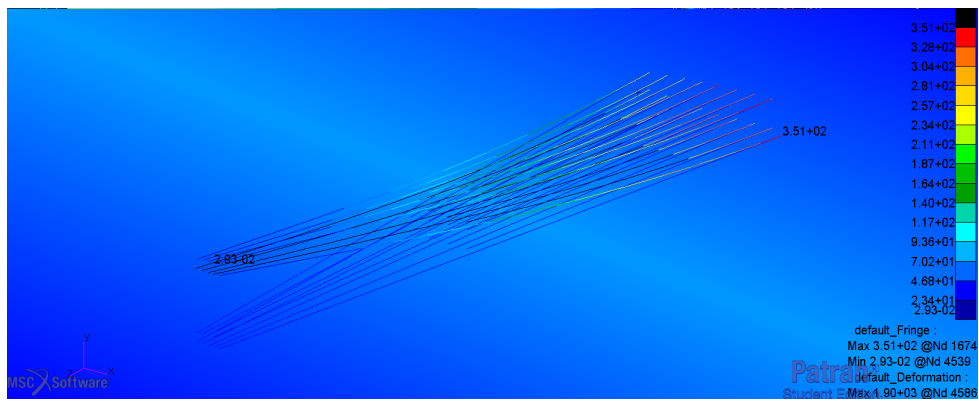Figure 5.9.   Stress on spars and ribs

Figure 5.10.   Stress on spars and ribs with control
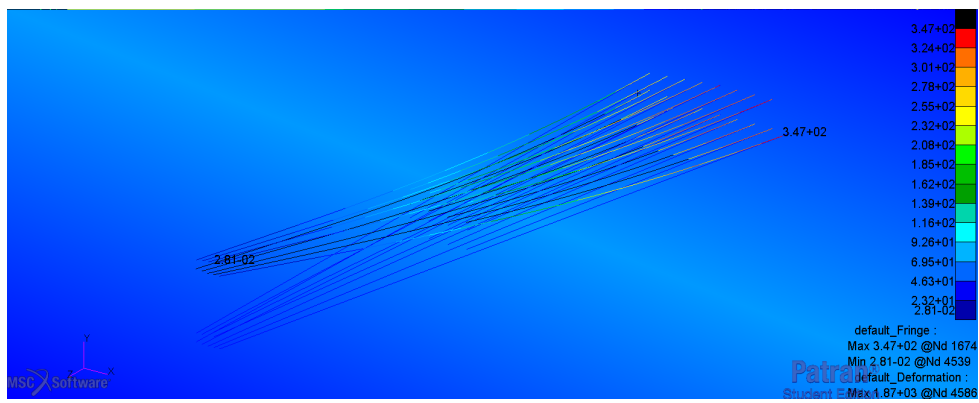

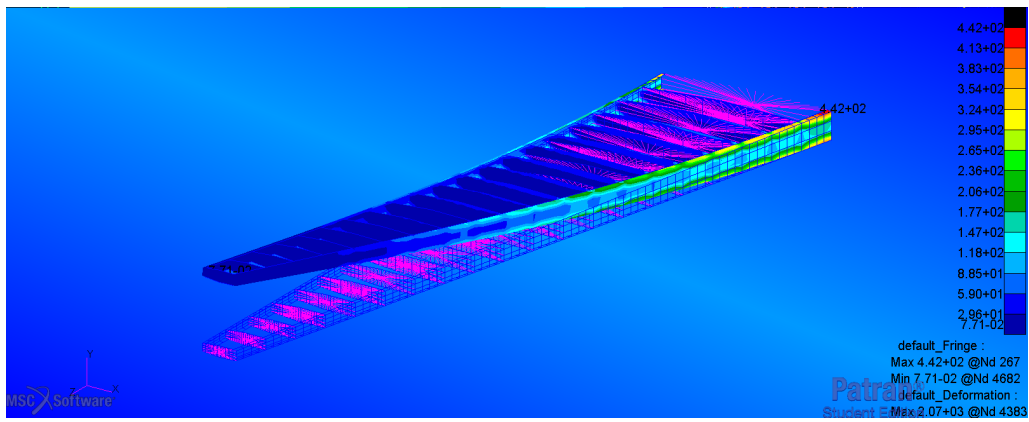Figure 5.11.   Stress on spars and ribs with control and reference signal

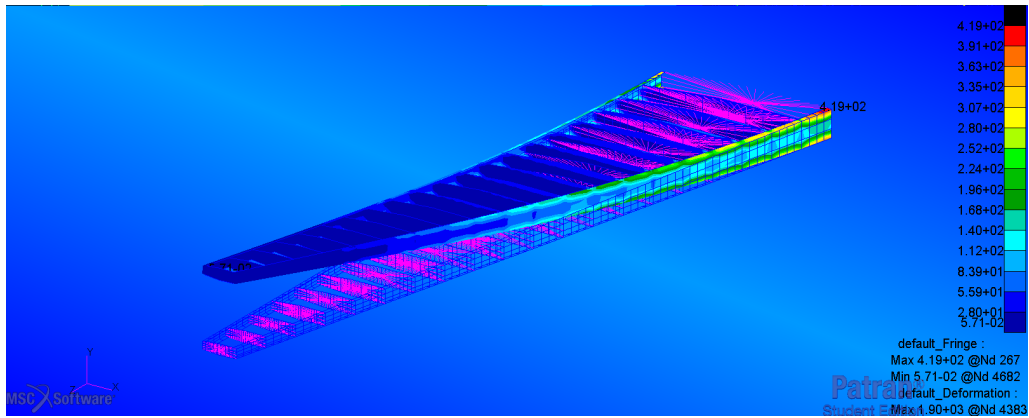Figure 5.12.   Stress on stringers

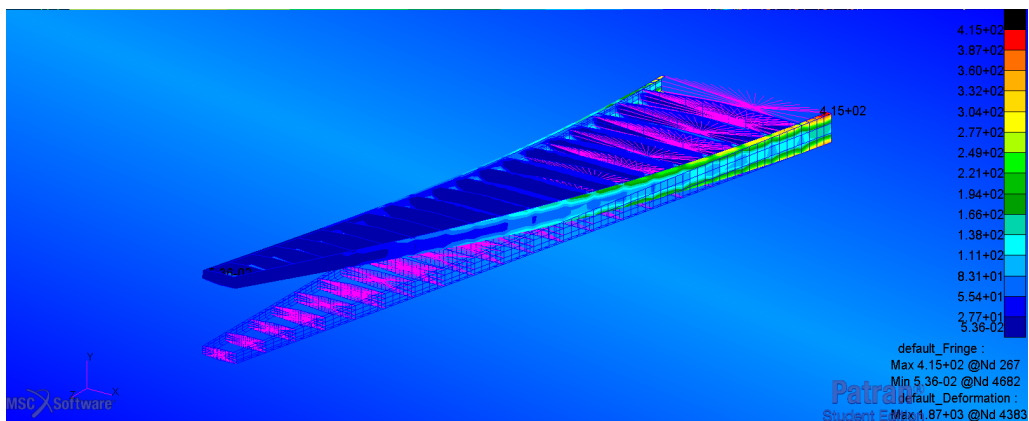Figure 5.13.   Stress on stringers with control

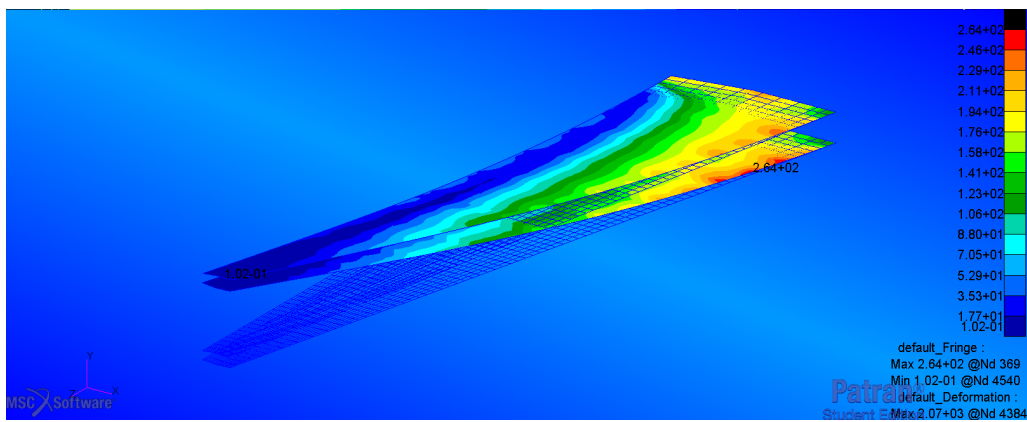Figure 5.14.   Stress on stringers with control and reference signal
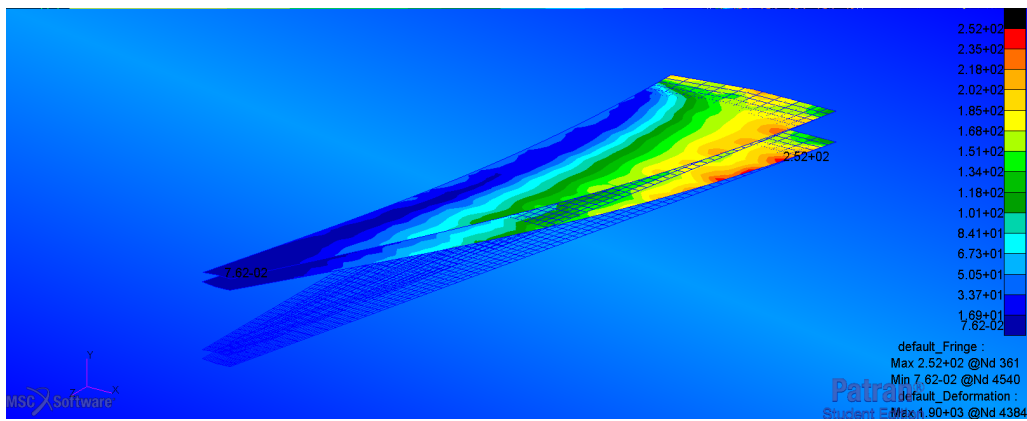
Figure 5.15.   Stress on skin panels

Figure 5.16.   Stress on skin panels with control
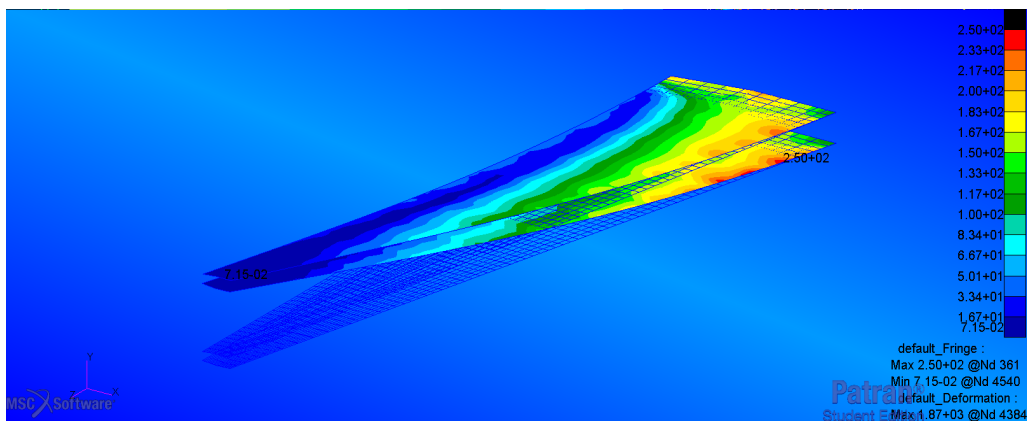

Figure 5.17.   Stress on skin panels with control and reference signal

Here below are also reported the data related to the stresses in the various elements that make up the structure, where are highlighted those in conditions of free deflection of the system, those of deflection with control of the displacement and those related to the control with the reference value.
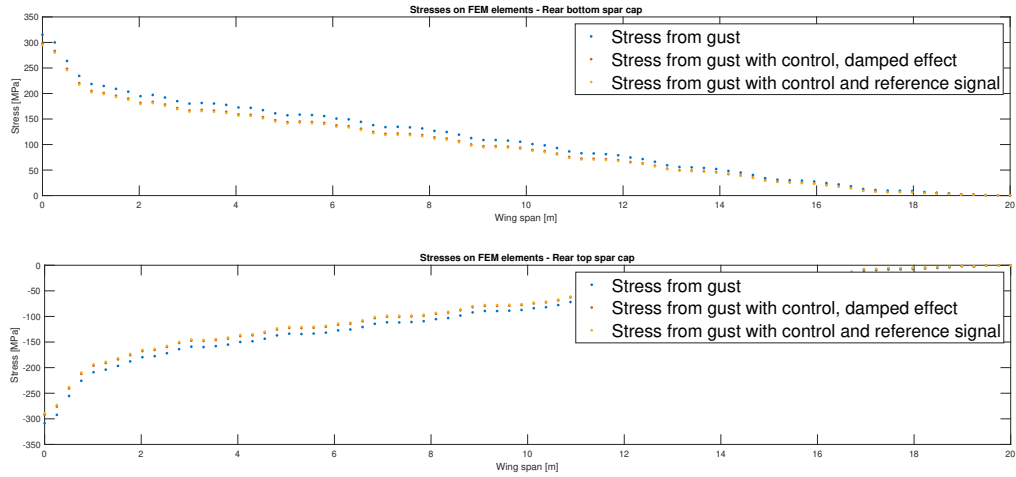

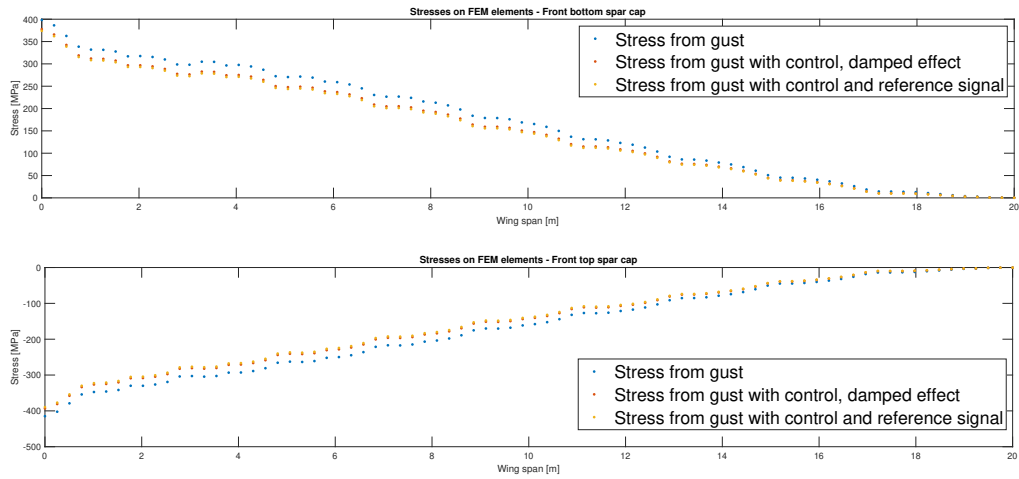Figure 5.18.   Stresses on the rear spar caps elements

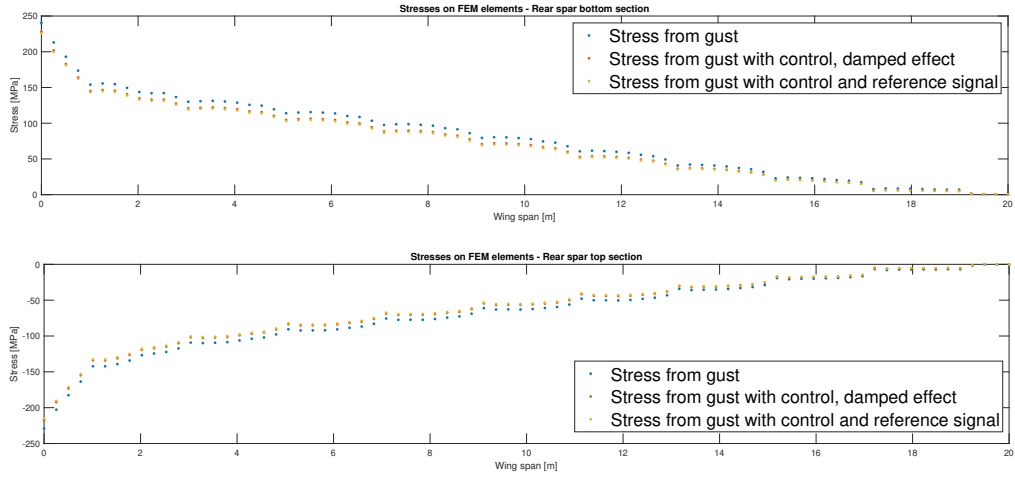Figure 5.19.   Stresses on the front spar caps elements

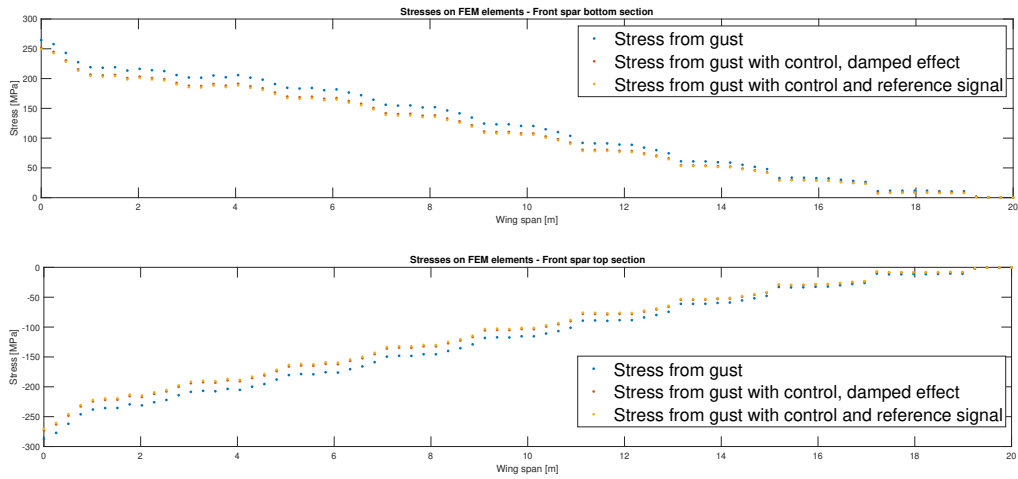Figure 5.20.   Stresses on the rear spar elements

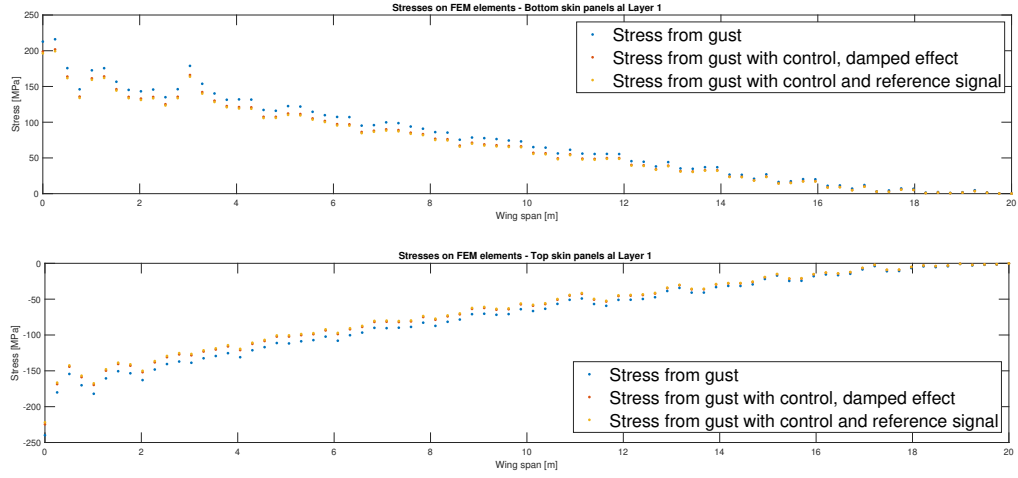Figure 5.21.   Stresses on the front spar elements

89

Figure 5.22.   Stresses on the skin panels elements

Part	Stress [MPa]	Stress with control [MPa]	Stress with control and reference signal [MPa]
Skin panels	$2.7320E+2$	$2.6096E+2$	$2.5877E+2$
Spar	$2.8720E+2$	$2.7306E+2$	$2.7054E+2$
Spar caps	$4.1484E+2$	$3.9332E+2$	$3.8948E+2$

Table 5.3.   Max stresses (σ_z) on structure parts

In the table 5.3 the values of the maximum stresses that can be reached in the three conditions of the system can be observed and a significant decrease of these stresses can be observed when a system deflection control is introduced, with reductions of stress that are shown in the table 5.3that go, with average values, from 10% to 14% in the various areas of the structure, which makes it even more understandable the importance and the usefulness of introducing a control on the deflections of the structure, which in this way can bear lower loads.

Part	Stress reduction with control %	Stress with control and reference signal %
Skin panels	10.82	12.74
Spar	10.70	12.61
Spar caps	12.22	14.39

Table 5.4.   Mean stresses (σ_z) reduction on structure parts

Chapter 6

Conclusions

A method for the reconstruction of the external loads for a wing is proposed. Moreover, a mitigation methodology is also designed, including a feedback control system based on mobile surfaces' deflection.

In Chapter 2 a preliminary research on the various types of sensors for strains and acceleration measurements has been performed. In this chapter, the methodologies for the displacement reconstruction are exposed. Two methods we proposed: starting (1) from deformations and (2) from accelerations. The criticalities of both methods are also introduced. The FEM model, used to perform analyses, is described in Chapter 3. In this chapter, concentrated and distributed loads are introduced. Finally, the reconstruction method for an equivalent reduced model is described, focusing on the properties needed to characterize it.

In chapter 4, as done previously, a method on the evaluation of the external loads from the strains measurement is derived, focusing on the reconstruction of the sensitivity matrix. A data optimization algorithm is presented, necessary to reduce the number of the strain gages required for an accurate reconstruction. The results of the reconstruction, with and without optimization, lead to reconstruction values with very low relative percentage error. In detail, an error of the order of $1E-3\,\%$ for the reconstructions using the optimization of the strain gauges, with a minimum number of measures, and errors of about $1E-4\,\%$ if the data of all the strain gauges are used. Since the error of the reconstruction is low, the methodology here proposed is validated. This result is important, since the number of the strain gages

needed will be higher than the minimum required, considering that come of them could be damaged during the time. The minimum number corresponds to the number of concentrated forces, or functions of the base in the case of distributed load. Is important, in choosing the right number, to take into account both the economic factor, linked to the number of detectors and the costs related to the installation, and the accuracy of the reconstruction to be performed. In chapter 5 a closed loop control system has been designed. The external perturbation, a gust disturbance, was defined, and a linear quadratic regulator (LQR) is proposed as control strategy. A control surface deflection is provided by the control system, and the variation of loads are analysed. The characteristics of the controller have been analysed, as well as the stability and controllability of the system once the controller has been introduced. From this analysis the reduction of the maximum internal stresses when a gust occurs is between 10% and 14%.

Since some assumptions have been made within this thesis, such as those concerning the distribution of forces or the damping definition, for future works it would be interesting to perform an aerodynamic and aeroelastic study of the wing, extrapolating the data related to the distribution of forces, including their variations with control surfaces. Furthermore it is possible to better evaluate the damping of the structure, introducing the one deriving from the aeroelastic analysis and include in the complete model all the wing structures and moving parts, carrying out a dynamic analysis of the complete structure subjected to a gust load in order to evaluate the impact and effectiveness of control through mobile surfaces.

Bibliography

[1] URL: https://www.hbm.com/en/4596/what-is-a-fiber-bragg-grating/.

[2] URL: https://en.wikipedia.org/wiki/Fiber_Bragg_grating.

[3] URL: https://www.fbgs.com/technology/fbg-principle/.

[4] URL: https://www.fiberoptictel.com/diy-fttx-projects-design-cables-splitting/fiber-cable-ribbon-laminate-construction/.

[5] URL: https://ifem.larc.nasa.gov/.

[6] URL: https://www.rotoview.com/accelerometer.htm.

[7] EASA - European Union Aviation Safety Agency. *Certification specifications, including airworthiness codes and acceptable means of compliance, for large aeroplanes CS-25*. 2003.

[8] R. Cirillo. "Detailed and condensed finite element models for dynamic analysis of a business jet aircraft". Tesi di laurea. POLITECNICO DI MILANO, 2011.

[9] Daniel L. Laird David J. Malcolm. "Extraction of Equivalent Beam Properties from Blade Models". In: *Wiley Interscience* (2006).

[10] Sangbo Han. "Measuring displacement signal with an accelerometer†". In: *Journal of Mechanical Science and Technology 24 (6) (2010) 1329 1335* (2010).

[11] Dipal Patelb Himanshu Mevadaa. "Experimental determination of structural damping of different materials". In: *Procedia Engineering 144 (2016) 110 – 115* (2016).

[12] O. Stodieck J.E. Cooper S.A. Neild M.H. Lowenberg L. Iorga. "Slender-Wing Beam Reduction Method for Gradient-Based Aeroelastic Design Optimization". In: *AIAA Journal, 56(11), 4529-4545* (2018).

[13]   Caughey T. K. and O'Kelly M. E. J. "Classical normal modes in damped linear dynamic systems". In: *Transaction of ASME, Journal of Applied Mechanics, 32, pp. 583–588* (1965).

[14]   Manfred Partl Martin Arraigada. "Calculation of displacements of measured accelerations, analysis of two accelerometers and application in road engineering". In: *Conference paper STRC 2006* (2006).

[15]   D. E. Newland. "Mechanical Vibration Analysis and Computation, Longman". In: *Harlow and John Wiley, New York* (1989).

[16]   Armando Pérez-Peña et al. "A methodology for damping measurement of engineering materials: application to a structure under bending and torsion loading". In: *Journal of Vibration and Control* (2016).

[17]   Michael Papadopoulos Piet Christof Wölcken, ed. *Smart Intelligent Aircraft Structures (SARISTU).* Springer International Publishing Switzerland, 2016.

[18]   Lord Rayleigh. "Theory of Sound (two volumes)". In: *Dover Publications, New York, reissued 1945, second edition* (1877).

[19]   Ernesto Zumelzu Roberto Pereira Jorge P. Arenas. "Comparison of four test methods to measure damping properties of materials by using piezoelectric transducers". In: *Materials and Design 32 (2011) 2423–2428* (2010).

[20]   Brian Rooks. "Automatic wing box assembly developments". In: *Industrial Robot: An International Journal, Volume 28 . Number 4 . 2001 . 297 - 301* (2001).

[21]   Li H.C.H. Herszeberg I. Davis C.E. Mouritz A.P. Galesa S.C. "Health monitoring of marine composite structural joints using fiber optic sensors". In: *Compos Struct 75; 321-327* (2006).

[22]   Wilber B. Huston T. H. Skopinski William S. Aiken. "Calibration of strain-gage installations in aircraft structures for the measurement of flight loads". In: *Langley Aeronautical Laboratory Langley Fielda, Va.* (1953).

[23]   Dakai Liang Xuegang Song. "Dynamic displacement prediction of beam structures using fiber bragg grating sensors". In: *Composite Structures 134 (2015) 762–771* (2017).

[24]   Jose Luis Mendoza Zabala. "State-Space Formulation for Structural Dynamics". In: *Submitted to the Department of Civil and Environmental Engineering on April 24, 1996, in partial fulfillment of the requirements for the degree of Master of Science in Civil and Environmental Engineering* (1996).